MIT Libraries | DSpace@MIT

MIT Open Access Articles

Mid-infrared integrated photonics on silicon: a perspective

Massachusetts Institute of Technology

Review article

Hongtao Lin*, Zhengqian Luo, Tian Gu, Lionel C. Kimerling, Kazumi Wada, Anu Agarwal
and Juejun Hu*

Mid-infrared integrated photonics on silicon: a perspective

Abstract: The emergence of silicon photonics over the past two decades has established silicon as a preferred substrate platform for photonic integration. While most silicon-based photonic components have so far been realized in the near-infrared (near-IR) telecommunication bands, the mid-infrared (mid-IR, 2–20-μm wavelength) band presents a significant growth opportunity for integrated photonics. In this review, we offer our perspective on the burgeoning field of mid-IR integrated photonics on silicon. A comprehensive survey on the state-of-the-art of key photonic devices such as waveguides, light sources, modulators, and detectors is presented. Furthermore, on-chip spectroscopic chemical sensing is quantitatively analyzed as an example of mid-IR photonic system integration based on these basic building blocks, and the constituent component choices are discussed and contrasted in the context of system performance and integration technologies.

Keywords: mid-IR; integrated photonics; silicon photonics; spectrometer; optical sensor.

*Corresponding authors: Hongtao Lin and Juejun Hu, Department of Materials Science and Engineering, Massachusetts Institute of Technology, Cambridge, MA 02139, USA; and Materials Processing Center, Massachusetts Institute of Technology, Cambridge, MA 02139, USA, e-mail: hometown@mit.edu (H. Lin); hujuejun@mit.edu (J. Hu).
http://orcid.org/0000-0001-7432-3644 (H. Lin)
Zhengqian Luo: Department of Materials Science and Engineering, Massachusetts Institute of Technology, Cambridge, MA 02139, USA; and Department of Electronic Engineering, Xiamen University, Xiamen 361005, China
Tian Gu and Anu Agarwal: Materials Processing Center, Massachusetts Institute of Technology, Cambridge, MA 02139, USA
Lionel C. Kimerling and Kazumi Wada: Department of Materials Science and Engineering, Massachusetts Institute of Technology, Cambridge, MA 02139, USA; and Materials Processing Center, Massachusetts Institute of Technology, Cambridge, MA 02139, USA

1 Introduction

Mid-IR (2–20-μm wavelength range) is a technologically important wave band [1–3] that (a) encompasses multiple atmospheric windows (e.g. 3–5 μm and 8–14 μm) essential for thermal imaging, infrared homing, and countermeasures and (b) covers the primary absorption bands of most chemical and biological molecules as well as the fingerprint region (7–20 μm), both of which are of prime interest to spectroscopic sensing. However, in contrast to their visible or near-IR counterparts, which carry much more energy per photon, mid-IR optical systems often suffer from inferior performance because they are far more susceptible to thermal fluctuations, often requiring cryogenic cooling. Mid-IR systems also generally use unconventional materials with less mature processing protocols, making production costs significantly higher. For instance, mid-IR optical components are made from germanium, diamond-turned silicon, chalcogenides, or halide crystals instead of standard optical materials such as oxide glasses and polymers, both of which become opaque in the mid-IR. Growth of narrow-band gap crystalline semiconductors for mid-IR optoelectronics requires exotic substrates such as off-cut Si, InSb, or CdZnTe.

Planar photonic devices obtained by integration onto a silicon platform offer a viable alternative for manufacturing low-cost and high-performance optoelectronics in high volumes. Leveraging standard semiconductor microfabrication technologies can dramatically decrease cost by taking advantage of the economies of scale. Integrated photonic devices are also capable of providing sub-wavelength-scale optical confinement to drastically boost light-matter interactions and signal-to-noise ratio (SNR). Moreover, integrated photonics affords unparalleled advantages in terms of size, weight, and power (SWaP) as well as robustness in comparison with systems assembled from discrete elements. In recent years, the capacity of photonic integration to reduce cost and improve performance has been validated in the field of optical communications, where integrated photonics solutions are now leading

high-bandwidth datacom transceiver products (e.g. Intel's 100G CWDM4 QSFP28). Expanding the operational wavelength of integrated photonic devices and systems to the mid-IR can revolutionize mid-IR optics and represents a prime growth opportunity for integrated photonics.

In this article, we present our perspective on the growing field of mid-IR integrated photonics. We choose to focus on photonic integration on silicon, the workhorse of microelectronics and silicon photonics for obvious reasons: silicon as a substrate features the unmatched combination of large size, superior mechanical ruggedness, remarkable chemical and thermal stability, low cost, as well as access to well-established fabrication infrastructure. Silicon also exhibits a high refractive index and a moderately broad transparency window in the mid-IR, up to around 7-μm wavelength, and is thus useful as a passive mid-IR optical material. However, unlike near-IR silicon photonics for telecom, which relies on standard silicon-based materials (Si, SiO_2, SiN, and Group IV alloys), a mid-IR integrated photonic system requires additional unconventional materials that are "hybrid-integrated" onto silicon. We note that the trend of new material incorporation is no stranger to the microelectronics industry, which initially used only a handful of elements in the 1980s but now has assimilated more than half the Mendeleev periodic table into their manufacturing process to keep pace with the scaling law. There is no reason to believe that microphotonics will be any different. This article seeks to provide a comprehensive review on state-of-the-art mid-IR devices integrated on silicon leveraging both monolithic and hybrid technologies, thereby including relevant material technologies beyond Si.

The review is sectioned by the device type and function, including the advantages and limitations of different device implementations. An on-chip spectroscopic sensor is then used as a model example to illustrate a mid-IR integrated sensor system design, which is optimized based on basic device building blocks. The design further yields quantitative insights into the chemical detection performance of such sensor-on-a-chip systems.

2 Waveguides and passive devices

Passive components made of optically transparent materials constitute the backbone in light-transmitting networks of a photonic circuit. In the mid-IR, opacity begins at the wavelength of onset of phonon absorption in materials. Consequently, extending the transparency window of a material in the mid-IR involves substitution of lighter elements with heavier ones to lower its characteristic
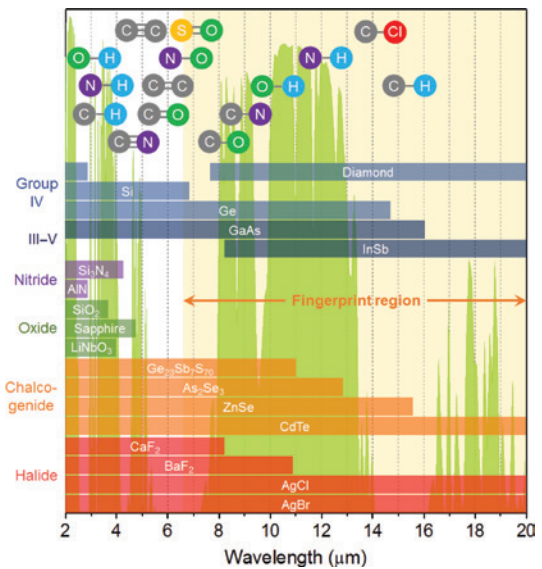

Figure 1: The mid-IR spectral regime: the bars represent optical transparency windows (where material attenuation is <1 dB/cm) of various materials, the top panel depicts the spectral locations of the primary absorption bands of different chemical bonds, and the background shows the infrared atmospheric transmission spectrum.

phonon frequency. This trend is evident from Figure 1, where we compare the transparency windows (defined as spectral regions where absorption is less than 1 dB/cm) of various optical materials. For example, Ge is a promising mid-IR waveguiding material with its high refractive index (n = 4.0) and IR transparency up to 14.6 μm, far exceeding that of Si (6.8 μm) [4]. Similarly, while oxides generally cannot transmit light beyond 5-μm wavelength, replacing oxygen with heavier chalcogens considerably extends the transmission window.

Data in Figure 1 allow photonic designers to make rational choices of passive material platforms across different parts of the mid-IR regime. For wavelengths shorter than 3.5 μm, standard silicon-on-insulator (SOI) or silicon nitride (SiN_x) on SiO_2 can be used because the silicon dioxide cladding remains optically transparent in this regime [5, 6]. At longer wavelengths, strong optical absorption in silicon dioxide compromises the optical performance of single-mode SOI wire waveguides [7]. Despite the onset of optical absorption in SiO_2, it is worth noting that low loss propagation can still be maintained in multi-mode or large-core ridge SOI waveguides at wavelengths above 3.5 μm, where strong modal confinement in the Si core leads to negligible absorption contribution from the cladding [8]. This is evident from Figure 2, which plots the simulated absorption losses in SOI waveguides with and without oxide top cladding and of two different core dimensions [9]. Modeling results show that SOI
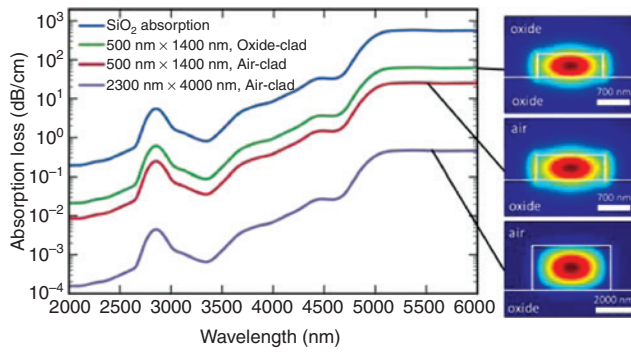
Figure 2: Calculated losses due to silicon dioxide absorption for different SOI waveguide layouts [9] (© 2017 Optical Society of America). The core sizes (height × width) and top cladding configuration are labeled, and the corresponding mode profiles are shown in the insets. Silicon dioxide absorption spectrum is also plotted for comparison.

waveguides with a large Si core and no oxide top cladding can effectively mitigate such parasitic optical losses. A remarkable intrinsic Q-factor exceeding one million

was attained at 3.8-μm wavelength in SOI micro-ring resonators following this design, although the multi-mode nature of the waveguide and the small evanescent field can limit its application in fields such as sensing.

To circumvent the limitation, several non-SOI platforms have also been explored. One strategy involves replacing the lossy silicon oxide cladding with other materials exemplified by silicon-on-nitride (Figure 3A–B) [10] and germanium-on-nitride [17] or with air cladding in pedestal [11, 18, 19] or suspended silicon structures [12–14, 20–23] (Figure 3C–H). Another option is Ge-on-Si (or SiGe-on-Si), which claims the advantage of compatibility with Si CMOS processing, as high-quality Ge can be epitaxially grown on Si (Figure 3I–J) [15, 17, 24–28]. Furthermore, the high index of Ge means that the Si substrate can function as the bottom cladding. In all these cases, the accessible wavelength is bound by the Si material absorption at approximately 7–8 μm. For photonic devices operating at even longer wavelengths, alternative materials other than
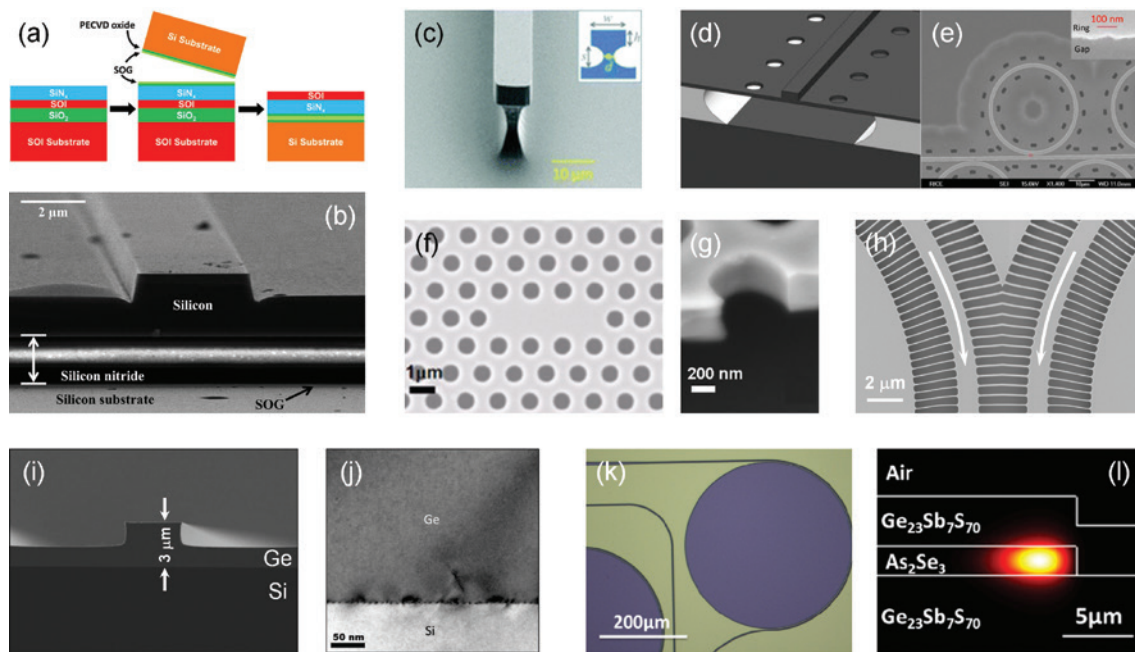

Figure 3: Examples of passive mid-IR photonic platforms.
(A, B) silicon-on-nitride [10] (© 2013 AIP Publishing LLC): (A) schematic fabrication process flow and (B) SEM tilted view of silicon-on-nitride mid-IR waveguides. (C–H) Pedestal or suspended Si devices: (C) SEM image of a pedestal mid-IR silicon waveguide. Reprinted with permission from [11], (D, E) schematic view and top-view SEM image of suspended Si mid-IR micro-ring resonators [12] (© 2013 Optical Society of America), the waveguides assume a ridge geometry and an undercut etch removes the silicon dioxide cladding through access holes on the slab layer, (F, G) SEM micrographs of a suspended mid-IR Si photonic crystal cavity [13] (© 2011 Optical Society of America), (H) suspended mid-IR Si waveguides with sub-wavelength grating (SWG) claddings [14] (© 2016 Optical Society of America); here the SWG provides both lateral optical confinement as well as access to the oxide under cladding during wet etch structure release; the arrows indicate light propagation direction in the suspended core. (I, J) Ge-on-Si [15] (© 2015 IEEE): (I) a mid-IR Ge-on-Si ridge waveguide; (J) TEM cross-sectional image of the Ge-on-Si film showing that the dislocations are confined at the Si/Ge interface. (K, L) Chalcogenide glass-on-silicon [16] (© 2013 Optical Society of America): (K) top-view optical micrograph of a ChG micro-disk resonator, (L) cross-sectional structure and simulated whispering gallery mode profile in the micro-disk at 5.2-μm wavelength; the high-index As_2Se_3 glass forms the core layer surrounded by low-index $Ge_{23}Sb_7S_{70}$ glass cladding.

Si are mandated. The recently demonstrated suspended Ge membrane devices hold the potential to fully utilize the broad transparency band of Ge, although optical functions of these devices at >3-μm wavelength are yet to be realized [29, 30]. Infrared-transparent chalcogenides and halides, on the other hand, can be monolithically deposited on Si or dielectric substrates via thermal evaporation or sputtering, with waveguides defined by using two compositions of different indices as core and cladding layers (Figure 3K–L) [16, 31–38]. Compared to Si or Ge, the drawback of this approach is that chalcogenides and halides are generally not considered compatible with CMOS foundry processes. However, the recent report of chalcogenide device integration with silicon waveguides indicates that such a hybrid configuration can enable seamless integration of unconventional materials with the standard silicon photonics platform [39].

Table 1 shows the available passive platforms for mid-IR integrated photonics on Si, including the best reported results on low loss performance obtained in each category. Although silicon-on-sapphire (SOS) [44–51] is not formed on a Si substrate, it is widely adopted for mid-IR photonics and is also included for comparison.

Besides simple optical waveguides, a wide array of other on-chip passive devices has already been demonstrated across the mid-IR band. Over the past few years, significant progress has been made in the fabrication process optimization of passive mid-IR photonic devices such that now their performance is comparable with their mature counterparts at telecom bands. Table 2 summarizes the current state-of-the-art for various passive components integrated on Si. Steady performance improvement is anticipated as silicon photonic manufacturing technologies continue to evolve.

3 Light sources and amplifiers

Light source integration on Si has always been a grand challenge for silicon photonics due to the indirect band gap of Si. In the mid-IR, the challenge is equally formidable; nevertheless, several potential routes have emerged. They include (1) heterogeneous integration of cascade lasers and diode lasers, (2) nonlinear frequency generation or conversion, and (3) heteroepitaxy of narrow gap semiconductors on Si. All three approaches have been experimentally validated and are capable of generating spatially coherent (single-mode) emission with high spectral brightness (defined as the emitted power per unit optical bandwidth).

3.1 Heterogeneous integration of cascade lasers and diode lasers

Quantum cascade lasers (QCLs) and interband cascade lasers (ICLs) have made substantial technological strides

Table 1: Passive waveguide platforms for the mid-IR.

Core material	Waveguide system	Cut-off wavelength (μm)[a]	Propagation loss in dB/cm (measurement wavelength)
Silicon	Silicon-on-insulator [5, 8, 40–43]	4.3	0.2 (3.8 μm) [9]
	Silicon-on-insulator (multi-mode) [9]	6.7	
	Silicon-on-porous silicon [5]	6.7	3.9 (3.39 μm) [5]
	Silicon-on-sapphire [44–51]	5.2	0.7 (4.5 μm) [48]
	Silicon-on-nitride [10]	5.5	5.2 (3.39 μm) [10]
	Suspended silicon [12–14, 20–23]	6.7	0.8 (3.8 μm) [14]
	Silicon pedestal [11, 18, 19]	6.7	2.7 (3.7 μm) [18]
Germanium	SiGe-on-silicon [52–56]	6.7	1.5 (4.6 μm) [56]
	Ge-on-silicon [15, 17, 24–28]	8.7	0.6 (3.8 μm) [27]
	Ge-on-SiO$_2$ [57]	4.3	1.4 (1.95 μm) [57]
	Ge-on-nitride [17]	5.5	3.4 (3.8 μm) [17]
Silicon nitride	Silicon nitride on SiO$_2$ [6, 58–60]	4.3	0.16 (2.6 μm) [60]
Chalcogenides	Chalcogenide glass on SiO$_2$ [31, 61, 62]	4.3	0.75 (3.6 μm) [31]
	Chalcogenide-on-silicon [16, 31–37]	19.2 [31]	0.3 (5 μm) [33]
Other materials	AlN-on-insulator [63]	2.8	0.8 (2.5 μm) [63]
	Diamond-on-insulator [64, 65]	2.9	2.9 (3.37 μm) [65]
	Halide on SiO$_2$ [38]	4.3	20 (10.6 μm) [38]

[a]The operational wavelength range of each waveguide system (except multi-mode SOI) is defined as the spectral regime where the total material absorption is <1 dB/cm, assuming that the confinement factor in the core is 110% and in the cladding 20%, close to the single-mode cut-off condition. Here the greater-than-unity confinement factor in the core manifests the slow light effect (see, for example, Robinson et al. [66]).

Table 2: Passive mid-IR components on Si and their state-of-the-art performance.

Component	Geometry	Material platform	Wavelength (µm)	Performance metrics (IL: insertion loss; Q: loaded Q-factor)	Reference
Waveguide	Strip	Silicon nitride on oxide	2.6	Loss = 0.16 dB/cm	[60]
		SOI	3.8	Loss = 0.2 dB/cm	[9]
		Chalcogenide glass-on-Si	5	Loss = 0.3 dB/cm	[33]
	Slot	SOI	3.8	Loss = 1.4 dB/cm	[42]
	Photonic crystal	SOI	3.4	Loss = 20 dB/cm	[40]
Fiber waveguide interface	Grating coupler	Suspended Si	2.7	IL = 6 dB	[67]
		Ge-on-Si	5.2	IL = 4 dB	[68]
		Suspended Ge	2.37	IL = 11 dB	[29]
	Inverse taper	SOI	2.5	IL = 9 dB	[69]
Splitter	Y-junction	AlN on oxide	2.6	IL not reported	[63]
	Multi-mode interferometer (MMI)	SOI	3.7	IL = 3.6 dB	[8]
		Ge-on-Si	3.8	IL = 0.21 dB	[15]
		Suspended Si	3.7	IL < 0.7 dB	[14]
	Directional coupler	SOI	3.7	IL not reported	[43]
Resonator	Micro-ring/micro-disk	Suspended Si	2.75	Q = 8100	[12, 20]
			5.2	Q = 2700	
		Multi-mode SOI	3.8	$Q = 1.1 \times 10^6$	[9]
		Silicon nitride on oxide	2.5	$Q = 10^6$	[60]
		Chalcogenide glass-on-Si	5.2	$Q = 10^5$	[16]
	Photonic crystal cavity	Suspended Si	4.4	Q = 13,600	[13]
		Suspended Ge	2.33	Q = 400	[30]

since their invention in the 1990s [70, 71]. Compared to traditional semiconductor laser diodes, QCLs and ICLs offer much wider wavelength coverage in the mid-IR. Cascade lasers operating in the continuous wave (CW) mode at room temperature cover almost the entire mid-IR spectrum (3–20 µm) and are now available as commercial off-the-shelf (COTS) components.

Heterogeneous integration of QCLs with Si photonics was first demonstrated by Spott et al. [72] and emits at around 4.8-µm wavelength. The substrate was a silicon-on-nitride-on-insulator wafer fabricated by bonding an SOI wafer to a nitride-on-insulator (SONOI) wafer. The III–V quantum cascade gain region was grown on an InP substrate and then flip-chip bonded onto the SONOI wafer on which passive Si waveguides were already defined, followed by substrate removal and III–V device mesa patterning on the Si waveguides. The resulting laser structure is shown in Figure 4A–C. The laser cavity is nominally located between two uncoated Si waveguide facets, although the authors implied that spurious reflections occurring at the III–V taper regions due to misalignment between the Si waveguide and the III–V mesa are strong enough to form a laser cavity. Figure 4D plots the laser output power and voltage versus drive current in two such devices at 20°C. The slope efficiency is 0.17 W/A, and the maximum wall plug efficiency is 0.35%, both measured from device B in

Figure 4D. The efficiency figures are considerably lower relative to those of state-of-the-art QCL lasers, suggesting significant room for design and processing optimization. The same group also demonstrated distributed feedback (DFB) QCL integration on Si following the same integration scheme [73].

At the shorter wavelength end of the mid-IR spectrum where room-temperature operation of cascade lasers is yet to be realized, classical diode lasers based on type-I or type-II semiconductor heterostructures offer an encouraging performance. For example, pulse mode laser emission up to 4-µm wavelength at room temperature was recently demonstrated utilizing GaSb type-II quantum well structures [74]. Several instances of heterogeneous integration of III–V mid-IR diode lasers and amplifiers with Si waveguides have been reported, including InP-based Fabry-Perot (F-P) and DFB lasers emitting at 2.0 µm [75] and 2.3 µm [76, 77], GaSb-based F-P laser operating at 2.38 µm [78], and InP-based optical amplifier at 2.0 µm [79]. Figure 5 depicts the structure of an InP-based multi-quantum-well (MQW) F-P laser on Si emitting at 2.3 µm [76], which exemplifies a large class of heterogeneously integrated III–V lasers. The III–V gain medium is die bonded onto a wafer with pre-fabricated Si waveguides and then patterned to define the III–V device mesa. The optical mode is transferred between the III–V gain region and a Si waveguide through adiabatic inverted taper couplers [80], and two
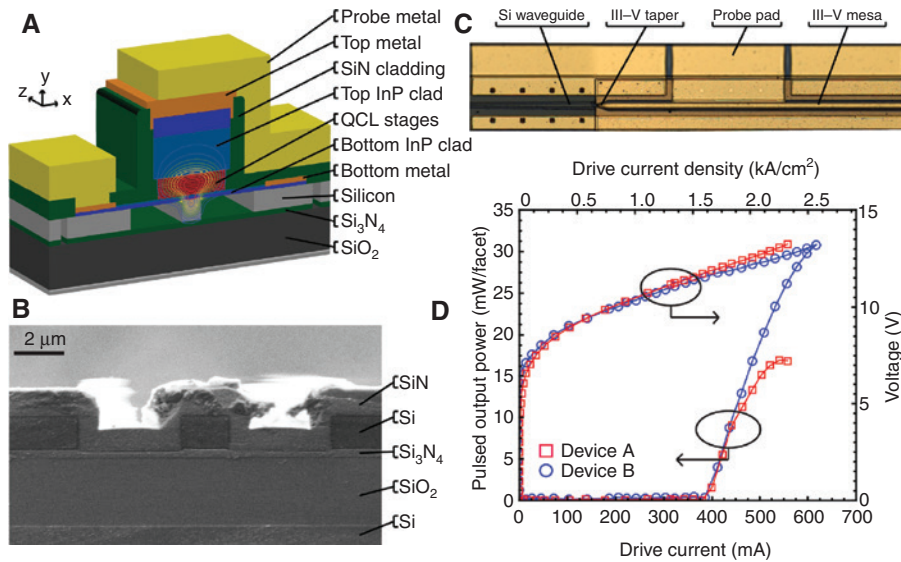
Figure 4: QCLs heterogeneously integrated on Si.
(A) Schematic diagram showing the structure of the active region of a heterogeneously integrated QCL, (B) SEM image of a polished SONOI waveguide facet, (C) top-view micrograph of the device, (D) output power and applied voltage versus drive current measured in two devices [72] (© 2016 Optical Society of America).
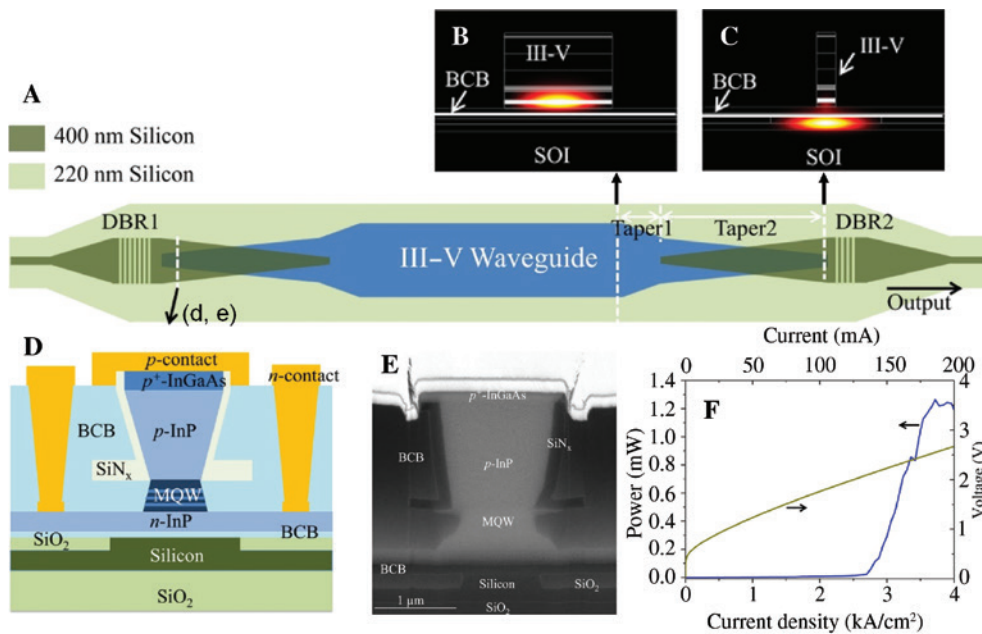

Figure 5: Heterogeneously integrated 2.3-μm laser.
(A) Top-view schematic depicting the heterogeneously integrated 2.3-μm laser layout; (B, C) optical modal profiles at different locations inside the laser cavity, the respective locations are marked with arrows in (A); (D) schematic and (E) SEM image showing the cross-sectional structure of the laser at the location marked with an arrow in (A); (F) measured output power and voltage versus injection current density of the laser [76] (© 2016 Optical Society of America).

Bragg grating reflectors engraved in the Si waveguide provide optical feedback for lasing. The laser exhibits a slope efficiency of ~1.7% near the threshold when operating in the CW mode at 5°C.

At present, the hybrid integrated mid-IR lasers (including the QCL on Si) are not broadband wavelength tunable. Work by Wang et al. [81] have demonstrated laser wavelength tuning over a 58-nm band centered at

2.04 µm by butt coupling a GaSb gain chip to a silicon photonic external cavity. The external cavity employs a pair of thermally tunable SOI micro-ring resonators for lasing wavelength selection via the Vernier effect. We expect that similar designs can be implemented to allow wavelength tuning of heterogeneously integrated mid-IR lasers across the gain bandwidth of the lasing medium. The same group also recently demonstrated a multi-wavelength DFB laser array on Si covering 2.28–2.43 µm, where the lasers are all fabricated from one bonded III–V die with their wavelengths controlled by SOI grating pitch [82].

A second approach to realize broad wavelength coverage on a single chip is to integrate multiple laser dies onto the same substrate [83]. In this case, the attainable bandwidth is no longer bound by the gain bandwidth of semiconductor structures but only by manufacturing complexity associated with multi-chip die bonding processes.

3.2 Nonlinear frequency generation or conversion

On-chip mid-IR light generation can leverage several nonlinear optical interactions, such as wavelength conversion using parametric processes, stimulated Raman scattering (SRS), and supercontinuum (SC) generation to translate light at near-IR wavelengths to the less accessible mid-IR domain or to expand spectral coverage of light sources in the mid-IR. Integrated photonics on Si is uniquely poised for nonlinear frequency generation or conversion in the mid-IR, as (1) the available material systems (including Si, Ge, SiN_x, and chalcogenide glasses) exhibit strong Kerr and Raman nonlinearities [84]; (2) in the mid-IR, detrimental nonlinear absorption effects such as two photon absorption (TPA) are subdued with decreasing photon energy, for example, TPA becomes negligible in silicon at wavelengths longer than 2.2 µm; and (3) strong optical confinement as a result of high-index-contrast and possibly optical resonance enhancement in integrated photonic devices can dramatically boost nonlinear interactions.

SRS was one of the first nonlinear interactions exploited towards on-chip light sources on Si. Crystalline semiconductors exhibit extraordinarily large Raman gain coefficients. For instance, Si has a Raman gain coefficient 10^3–10^4 times higher than that in silica optical fibers [85], which, when coupled with the small modal area and hence high optical intensity in Si waveguides, makes Si an attractive platform for Raman amplification and emission. Silicon waveguide Raman lasers have been demonstrated in the near-IR at around 1.6–1.7-µm wavelengths [86, 87] and up to 1.85 µm via cascaded Raman scattering [88]. Raghunathan et al. [89] further demonstrated a mid-IR Raman amplifier based on a bulk Si crystal, which reached a Stokes signal gain of 12 dB at 3.39-µm wavelength when pumped with a pulsed optical parametric oscillator source at 2.88 µm. Despite the advances and several follow-up theoretical investigations [90–92], mid-IR Raman lasing based on an on-chip Si platform has not yet been experimentally realized. As an alternative to Si, Raman lasing near 2.0-µm wavelength with an estimated internal quantum efficiency of 12% was achieved in diamond micro-resonators fabricated by transferring a diamond film onto an oxide-coated Si substrate [93]. In this case, the large Stokes shift in diamond (40 THz) versus that of Si (15.6 THz) facilitates first-order wavelength transition from telecom bands to the mid-IR range without resorting to the less efficient cascaded Raman scattering.

Besides Raman scattering, parametric conversion processes such as difference frequency generation (DFG) and four-wave mixing (FWM) can also be harnessed for mid-IR photon generation. As unstrained silicon and non-poled amorphous materials such as silicon nitride are structurally centrosymmetric and lack second-order nonlinear response (χ_2), FWM is the most commonly utilized parametric process in silicon photonics. Indeed, mid-IR light generation and amplification, up to 3.6-µm wavelength using both pulsed [94–97] and CW pump sources [98–100], capitalizing on first-order FWM in the SOI platform have been reported by several groups. Unlike SRS, FWM (as well as other parametric processes) mandates phase matching and judicious dispersion engineering of the nonlinear optical waveguide to maximize the gain bandwidth and conversion efficiency. For semi-standard SOI with 220-nm Si layer thickness, the optimal width for a Si waveguide operating near 2.1-µm wavelength was identified to be 900 nm, where, fortuitously, the second-order and fourth-order dispersion coefficients have opposite signs to facilitate broadband phase matching [101]. Using such waveguides, Kuyken et al. [102] measured optical parametric amplification (OPA) with 550-nm net gain bandwidth (centered at 2.17-µm pump wavelength) and an impressive 30-dB Raman-assisted peak off-chip gain (with FWM contribution exceeding 20 dB). Both metrics represent major improvements over the initial on-chip mid-IR OPA demonstration by the same group where a non-optimized waveguide design was used [103]. Dispersion engineering also contributes to enhanced power conversion efficiency (here defined as fraction of power converted from the
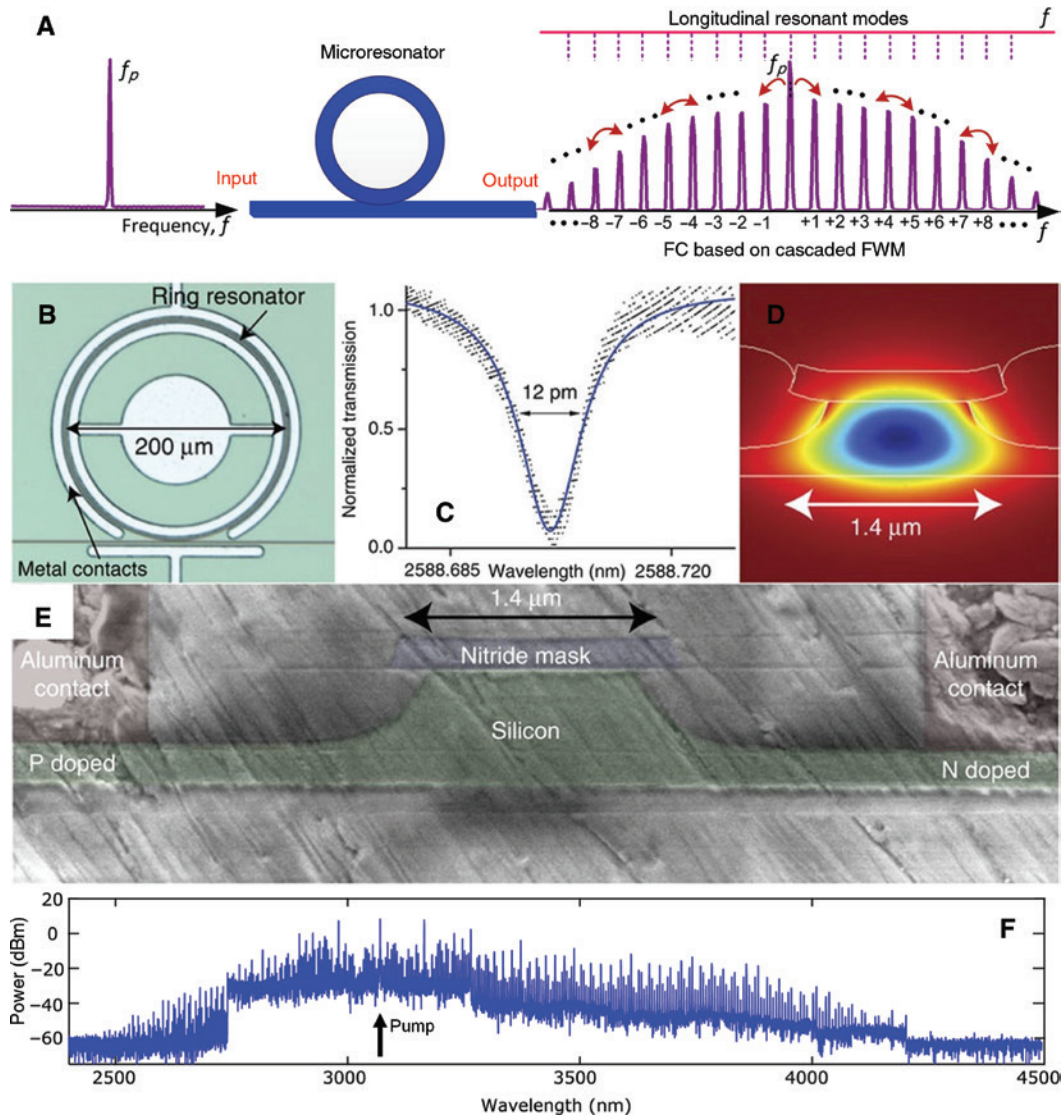
Figure 6: Mid-IR frequency comb generation in micro-resonators.
(A) Schematic illustration of the frequency comb generation process in a micro-resonator via cascaded FWM, (B) top-view of an etchless Si micro-ring resonator integrated with a p-i-n diode structure to sweep free carriers resulting from three photon absorption [69] (© 2015 Nature Publishing Group), (C) transmission spectra of the device near a resonant peak, (D) simulated optical mode and (E) SEM cross-sectional micrograph of the resonator waveguide, (F) mode-locked FC spanning 2.4–4.3 μm generated from the resonator device pumped at 3.07 μm; note that the significant pump depletion manifests the high power conversion efficiency (40%) of the FC [105] (© 2016 Optical Society of America).

single-frequency pump to the newly generated frequency lines[1]). Nevertheless, even the best reported power conversion efficiency figures in these first-order parametric conversion devices are still only around −30 dB [41, 100].

Micro-resonator-based optical frequency comb (FC) leverages cascaded FWM process to create a forest of evenly

---

1 The definition gauges the power efficiency of nonlinear on-chip sources on an equal footing with other light source technologies, e.g. lasers. Note that it differs from the nonlinear conversion efficiency typically quoted for OPA, which is given as the ratio of output idler power to the input signal power.

spaced spectral lines over a broad frequency domain [104]. To generate FC, a narrow-linewidth CW laser spectrally aligned to a resonant mode is injected into an on-chip resonator. The resonator supports a multitude of longitudinal resonance modes with equal frequency spacing. Degenerate FWM pumped by the CW source and amplified inside the resonant cavity produces symmetric sidebands aligned to the resonant modes, and parametric oscillations occur when the FWM gain of the excited resonant modes exceeds their loss rates. These sidebands can then serve as the pump sources for subsequent cascaded FWM processes into more resonant modes, as illustrated in Figure 6A.
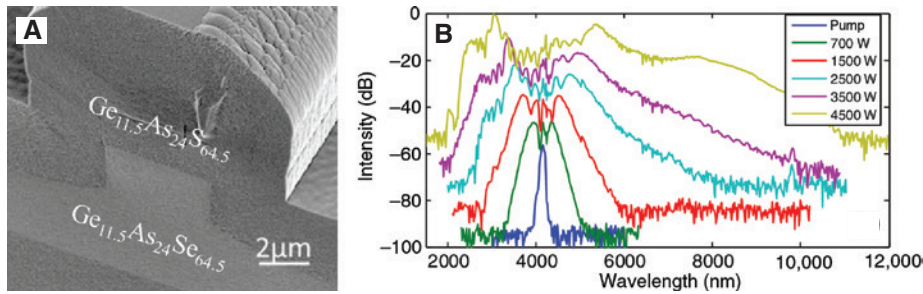
Figure 7: Mid-IR supercontinuum generation in chalcogenide glass waveguides.
(A) SEM image of a nonlinear mid-IR ChG waveguide, (B) spectra of supercontinuum generated from the waveguide at different pump peak power levels [115] (© 2016 Optical Society of America).

Mid-IR FC generation has been realized in both SOI and SiN$_x$ platforms (Figure 6) [60, 69, 105–107]. The most important figures of merit for FC include spectral bandwidth, noise, and power conversion efficiency. The comb bandwidth is primarily determined by pump peak power, nonlinear coefficient, as well as dispersion properties of the resonator [84]; the noise can be suppressed via mode-locking the comb into a single-soliton state [105, 108]; and high power conversion efficiency (e.g. 40% [105]) can be obtained by operating the resonator in an over-coupled regime. We also note that optimization of these metrics can sometimes impose contradictory requirements. For example, it has been shown that power conversion efficiency deteriorates with increasing comb bandwidth [109].

Supercontinuum (SC) generation is yet another third-order nonlinear process to create broadband and spatially coherent light suitable for coupling with integrated photonic circuits. It is typically accomplished by launching an intense laser pulse through a nonlinear waveguide device, where the pulse's optical spectrum is enormously broadened during propagation. The SC performance mainly depends on the peak power of pump pulse as well as dispersion and length of the waveguide. The basic mechanism of SC generation in nonlinear waveguides is high-order soliton fission as a result of self-phase modulation, cascaded Raman scattering and FWM, dispersive wave emission, and soliton self-frequency shift. Generally, spectral broadening towards short wavelengths is mainly attributed to dispersive wave emission and FWM, while soliton self-frequency shift and cascaded Raman scattering play a key role in long-wavelength broadening. For more details, we direct interested readers to monographs dedicated to this topic [110, 111]. Notably, when temporal coherence between pulses in a SC pulse train is preserved, the SC is in effect a frequency comb. Generation of such a coherent FC with octave-spanning bandwidth in an SOI waveguide has been experimentally validated [41].

Mid-IR SC generation has already been reported in a number of planar waveguide systems including SOI [112], a-Si [113], Si-on-sapphire [114], and chalcogenide glasses (ChGs) [34, 61]. In particular, broadband SC from 2.2 μm to 10.2 μm was demonstrated in a ridge waveguide made from $Ge_{11.5}As_{24}Se_{64.5}$ ChG core embedded inside a $Ge_{11.5}As_{24}S_{64.5}$ cladding and pumped by 330-fs pulses at a center wavelength of 4.184 μm (Figure 7) [115]. This impressive spectral coverage benefits from a unique combination of broad infrared transparency and large Kerr nonlinearity of ChG materials used to construct the waveguide, minimal dispersion through judicious waveguide design, and a femtosecond mid-IR source pumping scheme.

3.3 Heteroepitaxy of narrow gap semiconductors on Si

Heteroepitaxy, i.e. epitaxial growth of non-Si materials on Si, enables monolithic integration of devices on the Si platform while taking advantage of the superior optoelectronic properties of non-Si semiconductors. At the telecom band, heteroepitaxial growth has culminated in electrically pumped laser sources on Si based on n-doped Ge [116] and InAs/GaAs quantum dots [117]. In the mid-IR, lasing from heteroepitaxially grown structures on Si has also been achieved based on material systems including GaSb, GeSn, and lead salts. Table 3 summarizes the key attributes of the laser structures.

Major issues remain to be resolved before these laser structures can be implemented in a mid-IR integrated photonics platform. GeSn has been hailed as a promising Group IV gain material with its direct band gap nature. Remarkable strides in GeSn-on-Si growth and device fabrication have been made over the past few years. Nevertheless, GeSn lasers demonstrated thus far are optically pumped, operate only in pulse mode and at low temperatures, and require large pumping threshold power density

Table 3: Mid-IR laser structures monolithically grown on Si via heteroepitaxy.

Active medium	Substrate orientation	Reference	Wavelength (μm)	Pumping scheme	Output mode	Maximum operation temperature (K)
GaInAsSb	Off-axis	[118]	2.25	Electrical	Pulse	≥300
		[119]	2.0	Electrical	CW	308
GeSn	(100)	[120]	2.25	Optical	Pulse	90
		[121]	2.4–2.5	Optical	Pulse	130
		[122]	2.5	Optical	Pulse	110
		[123]	3.1	Optical	Pulse	180
PbSe	(111)	[124]	3.5	Optical	Pulse	≥300
		[125]	3.3–5.1	Optical	Pulse	325
PbTe	(111)	[126]	3.6–5.3	Optical	CW	133 (CW)
					Pulse	273 (Pulse)

in the order of 100 kW/cm². The lead salt lasers are similarly optically pumped and mostly count on free-space external cavities to provide optical feedback (with the only exception of a photonic crystal surface emitting laser [124]). Among these material systems, GaSb-on-Si is probably the most advanced in terms of laser device development, providing electrically pumped CW lasing at room temperature with a wall plug efficiency close to 0.6% [119]. However, the laser structure is grown on an off-cut Si wafer to avoid the formation of antiphase domains, a fundamental issue often encountered in III–V heteroepitaxy on Si due to the non-polar nature of Si surface [127]. The need for an off-cut wafer with custom orientation is unfortunately not compatible with most integrated photonics applications. Moreover, technologies for integrating the lasers with other planar photonic circuit elements are yet to be developed.

Heteroepitaxially grown Ge/SiGe-on-Si structures have also been employed in terahertz quantum cascade electroluminescent emitters [128]. As the small conduction band offset between Si and Ge does not support cascade carrier relaxation, these emitters operate on intersubband transitions of holes instead of electrons. This is a chief shortcoming of this approach, limited by the larger effective mass of holes and a weak confinement potential. The prospect of mid-IR lasing in Si/Ge heterostructures remains challenging in light of these technical difficulties.

3.4 Other approaches

Alternative technical solutions for mid-IR light sources include thermal emitters and extrinsic doping with luminescent materials (e.g. transition metal ion, rare earth ions, or quantum dots [129]). While black body emitters are widely deployed as broadband infrared sources in free-space optics, coupling the spatially incoherent

radiation into a waveguide poses a fundamental limit to the useful power. The maximum spectral power density (PSD) of thermal radiation coupling into a single guided mode along one direction P_λ is given by [130]:

$$P_\lambda(T) = \frac{hc^2}{\lambda^3 \left[\exp\left(\frac{hc}{\lambda k_B T} \right) - 1 \right]}, \tag{1}$$

where T denotes the thermodynamic temperature of the emitter, h is the Planck constant, c represents the speed of light in vacuum, λ gives the free-space wavelength of thermal radiation, and k_B symbolizes the Boltzmann constant. The function is plotted in Figure 8 for several emitter temperatures. We see that even at an extremely high emitter temperature of 3000 K (close to hot electron temperature in a graphene emitter [131]), the PSD of thermal radiation is still merely of the order of 0.1 nW/nm in the mid-IR, far smaller than the attainable PSD of other types of light sources discussed here.

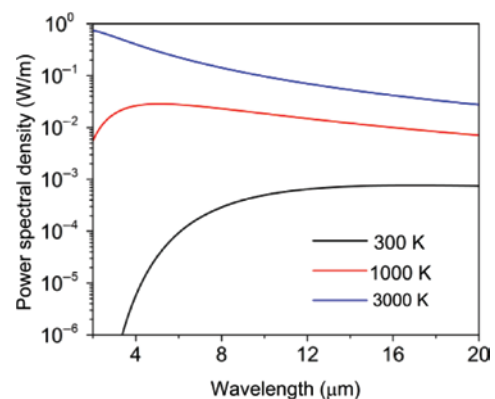In the category of extrinsic emitters relying on luminescent dopants, Cr- or Fe-doped ZnSe/ZnS (for emission

Figure 8: Power spectral density of a single-mode ideal black body emitter at various temperatures according to Eq. (1).

Table 4: Comparison of mid-IR on-chip light emitter technologies.[a]

Technology	Monolithic integration	Spatial coherency	Wavelength range (μm)	CW output	Electrical pumping	CW optical pumping	Broadband output
Heterogeneous integration	N	Y	2–20	Y	Y	Y	N/A
Frequency comb	Y	Y	2–20	N	N	Y	Y
Supercontinuum	Y	Y	2–20	N	N	N	Y
Heteroepitaxy[b]	Y	Y	2–5	Y	N/A	Y	N/A
Thermal emitter	Y	N	2–20	Y	Y	Not applicable	Y
Extrinsic doping	N/A	Y	2–5	Y	N	Y	N/A

[a]Y, technology is already available; N/A, while in principle possible, the technology has not yet been demonstrated; N, technologically infeasible or unlikely to be realized.
[b]Here we only consider heteroepitaxy on on-axis Si wafers.

between 2 and 5 μm) and Tm-doped tellurite glasses (at around 2-μm wavelength) rank among the favorable candidates. In both systems, amplification and lasing have been realized in non-Si platforms [132–135]. However, technical barriers remain towards electrical pumping in these systems [136], and integration technologies of these materials with Si are still under early stage development [31, 137–140]. Remarkable progress was also made in rare-earth doped fluoride glass fiber lasers with emission wavelengths up to 4 μm [141], although integration of multi-component fluorides on Si faces conceivable difficulties given their low refractive index, complex chemical compositions, and hygroscopic nature.

3.5 Summary and outlook

Table 4 compares the mid-IR light source technologies discussed above. Clearly, none of the technologies meet all the requirements listed. While considerable efforts are needed to improve device efficiency, yield, and integration capacity, it appears that heterogeneous integration is the most promising route towards high-brightness, single-frequency source integration on Si in the mid-IR. Meanwhile, micro-resonator-based FC nicely complements the hybrid lasers with its broad spectral span ideally suited for applications such as precision spectroscopy. A key advantage of FC over SC as a wide band emitter is that FC works with CW pump and does not require high-power, ultrafast pulses as the pumping source, as high-Q micro-resonators can provide the dramatic light intensity amplification necessary for strong nonlinear interactions through resonant cavity enhancement. In particular, we envision that heterogeneously integrated lasers can be used as optical pumps in conjunction with on-chip resonators to enable fully integrated, spatially coherent broadband comb sources.

4 Optical modulators and switches

Optical modulators are vital components of a photonic circuit to enable signal switching and routing, data encoding, phase-sensitive detection, and even spectroscopic interrogation, as we discuss later. In the near-IR telecom bands, optical modulators and switches generally operate using one of the following mechanisms: electroabsorption, free carrier plasma dispersion, thermo-optic effect, electro-refractive effects (e.g. Pockels effect), or acousto-optic effect. While most of these effects still prevail in the mid-IR regime, wavelength scaling can have a consequential impact on their modulation performance. In this section, we analyze the efficacy of different modulation mechanisms in the mid-IR and review examples of mid-IR modulator and switch devices already demonstrated. Here our emphasis is on waveguide-integrated devices on Si, and we exclude free-space modulators, as the latter are not amenable to planar photonic integration.

4.1 Thermo-optic switches

Thermo-optic coefficient, which describes the temperature-dependent refractive index variation of a material, has a relatively weak spectral dependence within the material's transparency window. Thermo-optic switching is therefore an equally useful modulation scheme in the mid-IR as in the telecom bands. To examine the influence of wavelength scaling on thermo-optic devices, we consider the thermo-optic figure of merit (FOM) defined as the inverse of the product of 10–90% rise time (t_r) and power consumption to turn on or off the switch (P_φ), a parameter often cited when drawing a comparison between different thermo-optic switching technologies. For a device based on the Mach Zehnder interferometer (MZI) configuration, the FOM is given as [142]:

$$\text{FOM} = \frac{1}{P_\varphi \cdot t_r} = \frac{0.9 n_g L}{\lambda C} \cdot \left(\frac{dn}{dT}\right)_{\text{eff}}, \qquad (2)$$

where n_g, L, C, and $(dn/dT)_{\text{eff}}$ denote the interferometer waveguide group index, length of the heated waveguide section in an MZI arm, lumped heat capacity of the heating zone, and effective thermo-optic coefficient of the waveguide, respectively. As a first-order approximation, L scales with λ and C scales with λ^3 and thus the FOM roughly follow a $1/\lambda^3$ scaling trend with wavelength as a result of the increased device volume in the mid-IR. We also note that slow light designs (large n_g) are an effective route to enhance the FOM, as previously validated in near-IR devices [143]. In a resonator-based thermo-optic switch, analysis yields [142]:

$$\text{FOM} = \frac{1}{P_\varphi \cdot t_r} = \frac{0.14 Q}{C} \cdot \left(\frac{dn}{dT}\right)_{\text{eff}}, \qquad (3)$$

where Q is the resonator Q-factor. Similarly to the MZI devices, the FOM of resonator-based thermo-optic switches also follows an approximate $1/\lambda^3$ dependence on wavelength. However, slow light has little impact on the FOM; instead, increasing Q-factor is the key to improving resonator switch performance.

Mid-IR integrated thermo-optic modulators have already been fabricated in SOI [144], Ge-on-Si [145], and silicon-on-sapphire [146]. Figure 9 shows one example of a SOI-based MZI switch [144]. The MZI arms are configured with a spiral geometry to increase the arm length L while minimizing thermal mass C. The device features a switching power of 47 mW and a 3-dB bandwidth of about 20 kHz, which correspond to an FOM of 0.0012 mW^{-1} μs^{-1}. Considering the $1/\lambda^3$ scaling factor, the FOM is comparable to that of MZI thermo-optic switches in the near-IR [147]. As discussed above, the device performance can be further improved by introducing slow light enhancement.

4.2 Electro-optic modulators utilizing the Pockels effect

Compared to the relatively slow thermo-optic modulation whose response time is typically in the microsecond regime, electro-optic effects are electronic in nature and thus offer ultrafast response in the femtosecond range. As discussed in preceding sections, common Si-based materials (Si, SiO$_2$, and SiN$_x$) lack second-order nonlinearity, and hence, electro-optic modulators on Si usually involve heterogeneous integration of other materials. For instance, electro-optic crystals (e.g. LiNbO$_3$) can be hybrid-bonded onto Si to confer Pockels activity. In the near-IR, LiNbO$_3$ integration has been accomplished via direct LiNbO$_3$ bonding onto SOI photonic circuits [148] or LiNbO$_3$ membrane bonding onto oxidized Si wafers followed by strip-loaded waveguide fabrication on top [149]. Mid-IR modulation has also been demonstrated in a Si-on-LiNbO$_3$ platform with an extinction ratio of ~8 dB, a half-wave voltage-length product ($V_\pi \cdot L$) of 26 V cm, and an insertion loss of 3.3 dB at 3.39-μm wavelength [150]. The same technology can be readily adapted for on-Si integration.

Besides heterogeneous integration, strain also imparts electro-optic activity to Si (albeit considerably smaller than that of LiNbO$_3$) [151, 152]. While the strained Si technology has not yet been applied to mid-IR modulators, the telecom band strained Si device architectures can be scaled to longer wavelengths.

One potential drawback with the electro-optic modulators is the large $V_\pi \cdot L$, which implies either a long device length (centimeters) or a high driving voltage (tens of volts). If we assume a weakly wavelength-dependent electro-optic coefficient [153], the product $V_\pi \cdot L$ approximately scales with λ^2 because the increase in device size at longer wavelengths requires higher driving voltage to maintain the same electric field. Accordingly, the limitation becomes
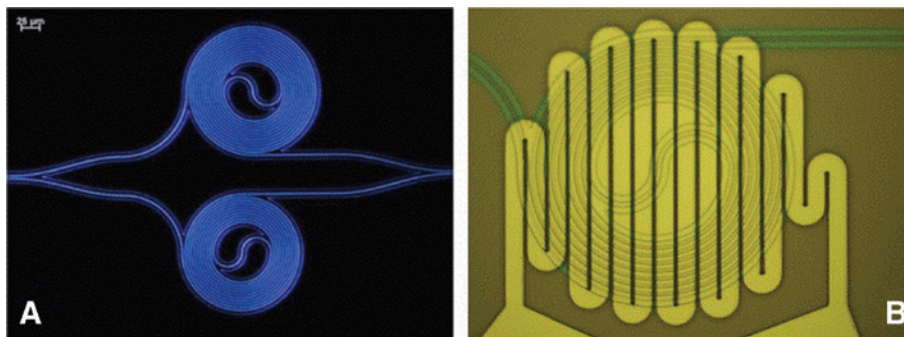

Figure 9: Mid-IR thermo-optic modulator.
Top-view optical microscope image of (A) a spiral-arm MZI thermo-optic modulator in SOI and (B) one arm of the spiral MZI with metal heaters [144] (© 2014 IEEE).

even more restricting at longer wavelengths. In addition, the accessible wavelength of current modulator designs is ultimately bound by optical transparency windows of electro-optic crystals, which are mostly oxides. New materials with stronger electro-optic response and broad infrared transmission window while amenable to silicon integration are essential for next-generation mid-IR electro-optic modulators.

4.3 Modulators based on free carrier plasma dispersion

Free carrier density modulation is known to modify the refractive index as well as extinction coefficient of materials. Simplistically, the free carrier induced index change (Δn) and free carrier absorption (FCA, denoted by the extinction coefficient change Δk) are described using the classical Drude model:

$$\Delta n = -\frac{e^2 \lambda^2}{8\pi^2 c^2 \varepsilon_0 n} \cdot \left(\frac{\Delta N_e}{m_e^\star} + \frac{\Delta N_h}{m_h^\star} \right), \qquad (4)$$

and

$$\Delta k = \frac{e^3 \lambda^3}{16\pi^3 c^3 \varepsilon_0 n} \cdot \left(\frac{\Delta N_e}{m_e^{\star 2} \mu_e} + \frac{\Delta N_h}{m_h^{\star 2} \mu_h} \right). \qquad (5)$$

Here e is the elementary charge, ε_0 represents the vacuum permittivity, n is the unperturbed refractive index of the material, ΔN is the charge carrier density, $m^\star$ denotes the carrier effective mass, and the subscripts e and h label quantities associated with electrons and holes, respectively.

Although the Drude model is oversimplified, it nevertheless yields useful insights on the wavelength scaling characteristics of free-carrier-based modulators.

There are two modulation modes capitalizing on the free carrier effects: an electro-optic or electro-refractive mode, which leverages Δn for phase modulation, and an electroabsorption mode utilizing Δk to generate intensity modulation. In both cases, carrier injection or removal is usually performed using a p-n junction or a metal-insulator-semiconductor (MIS) structure. If the p-n junction doping profile or the MIS gate dielectric layer thickness is kept constant, the capacitance per unit area remains unchanged. Under this assumption, the charge accumulation (or depletion) per unit area at a given bias voltage is fixed. Coupled with the λ^2 dependence of Δn (λ^3 for Δk), the assumption specifies a linear scaling behavior with λ for effective index (and quadratic scaling for absorption modulation) of the waveguide mode, as modal overlap with the carrier accumulation region scales with $1/\lambda$. The conclusion suggests that the $V_\pi \cdot L$ product of an electro-optic modulator stays nearly constant independent of wavelength. However, the electro-optic modulation FOM $-\Delta n/\Delta k$ diminishes as $1/\lambda$ with increasing wavelength, indicating that rising insertion loss precludes efficient operation of free-carrier-based electro-optic modulators at long wavelengths. On the other hand, electroabsorption modulators based on FCA can garner significant performance benefits from extending the operation wavelength to the mid-IR, as both the device length and the driving voltage can be reduced at longer wavelengths.

More detailed analysis by Nedeljkovic et al. [154, 155] reveals deficiencies of the Drude model when applied to real material systems such as Si and Ge (Figure 10). The Drude model does not take into account intervalence band transitions, which is pronounced in p-type Ge. The model also fails to predict saturation of free-carrier-induced index change and FCA at wavelengths above 10 μm and large carrier concentrations. Nevertheless, the refined
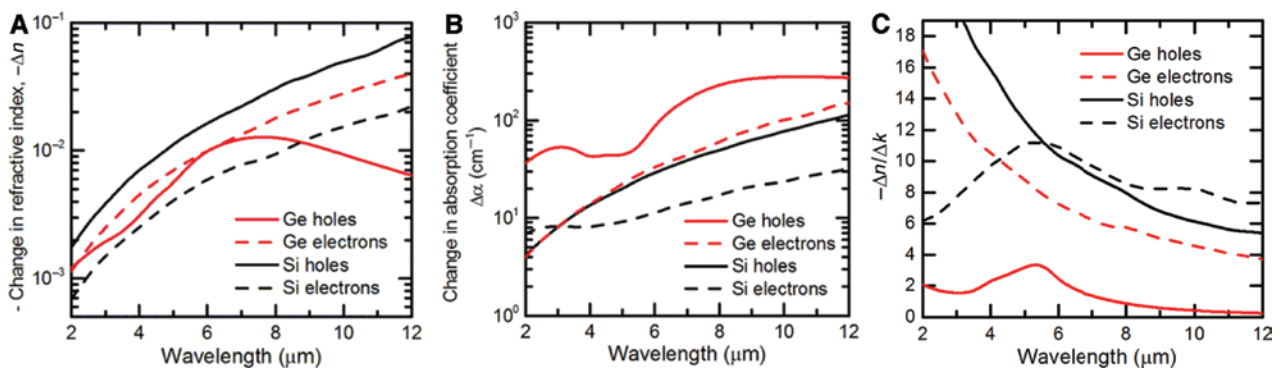

Figure 10: Free-carrier-induced changes of (A) refractive index and (B) absorption coefficient in Si and Ge in the mid-IR; (C) wavelength scaling of the electro-optic modulation FOM $-\Delta n/\Delta k$ computed from data in (A) and (B) [155] (© 2015 IEEE).
The data were quoted for a fixed carrier concentration of 5×10^{17} cm^{-3}.

analysis similarly points to the conclusion that while free-carrier-based electro-optic modulation remains effective between 2 and 3 μm, FCA is better suited for mid-IR modulation above 3-μm wavelength.

Both electro-optic and electroabsorption modulation exploiting free carrier effects have been implemented in the 2–2.5-μm band in SOI devices [156, 157], and all-optical modulation based on FCA was also demonstrated in Ge-on-Si waveguides [158]. At 2.165 μm, the electro-optic modulator achieved an impressive $V_{\pi} \cdot L$ of 0.012 V cm, an extinction ratio of 23 dB, and modulation bitrates up to 3 Gbps [156]. Improved efficacy of FCA modulation at longer wavelength was experimentally validated in the 2–2.5-μm and 3.8-μm bands [157, 159].

4.4 Electroabsorption modulators based on Pauli blocking or field-induced effects

The modulation mechanisms discussed in this section encompass two categories: field-induced absorption change such as Franz-Keldysh effect (FKE) and quantum confined Stark effect (QCSE) and absorption modulation due to band filling, i.e. Pauli blocking or Burstein-Moss shift.

Both FKE and QCSE use electric field applied to a semiconductor material to engender spectral shift of its absorption edge, and thus the devices necessarily involve narrow-gap semiconductors for mid-IR modulation. For instance, GeSn modulators operating on FKE have been theoretically investigated [160, 161], although experimental validation of such devices has not yet been reported. Narrow-gap Van der Waals solids such as black phosphorus (BP) present another choice for on-Si mid-IR modulators. Theoretical analysis shows that optical modulation in BP stems from both quantum confined

FKE and Pauli blocking, where their relative magnitude depends on BP layer thickness, doping, field strength, and wavelength [162]. Free-space optical modulation has recently been materialized where light is incident on the BP flake from a surface-normal direction [163, 164]. The small modulation extinction ratio (a few percentage) because of the short optical path length in few-layer BP can be overcome by adopting a waveguide-integrated architecture.

Graphene represents an excellent material platform for electroabsorption modulation harnessing Pauli blocking due to band filling. State-of-the-art graphene waveguide modulators have reached a remarkable 3-dB bandwidth of 35 GHz and a modulation depth of 70 dB/mm near the 1550-nm telecom band [165]. In the mid-IR, our group has recently demonstrated the first graphene-based waveguide modulator [142]. Figure 11A sketches the device layout, which comprises a ChG waveguide and two embedded graphene layers. In this design, the ChG material acts as both the light-guiding medium and the gate dielectric. The graphene layers are p-doped such that at zero bias, both are transparent to mid-IR light due to Pauli blocking. When a bias is applied across the chalcogenide gate, charge transfer between the two graphene sheets causes shift of their Fermi levels in opposite directions, resulting in onset of optical absorption in one of them as the condition for Pauli blocking breaks down. The prototype device exhibits a modulation depth up to 8 dB/mm at 2.05-μm wavelength (Figure 11B), which agrees well with our theoretical predictions derived from the surface conductive model (Figure 11C) [166].

Here we further extend our model to quantitatively project the performance of graphene electroabsorption modulators across the mid-IR band. As a starting point, Figure 12A plots the optical absorption in monolayer graphene in the mid-IR as a function of graphene Fermi level
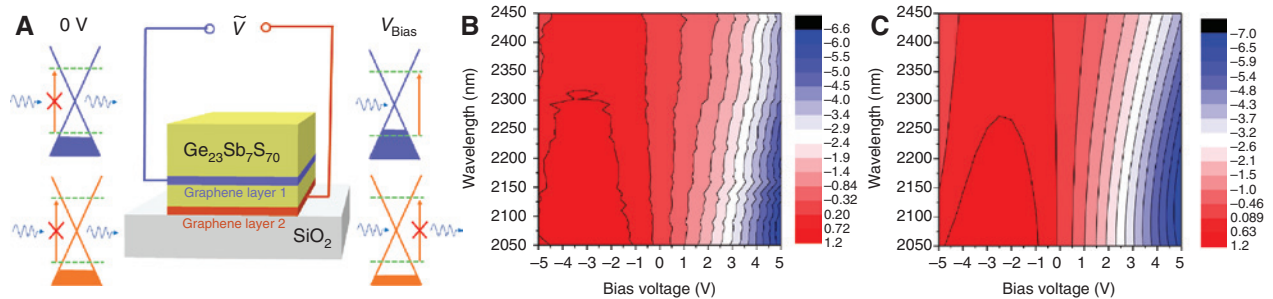

Figure 11: Graphene mid-IR waveguide modulator.
(A) Center: schematic diagram of the graphene mid-IR waveguide modulator; left and right: band profiles of the two graphene layers, where the arrows represent energy of incident photons; (B) measured and (C) simulated color contour maps showing wavelength and bias dependent modulation depth of the device in dB/mm [142] (© 2017 Nature Publishing Group).
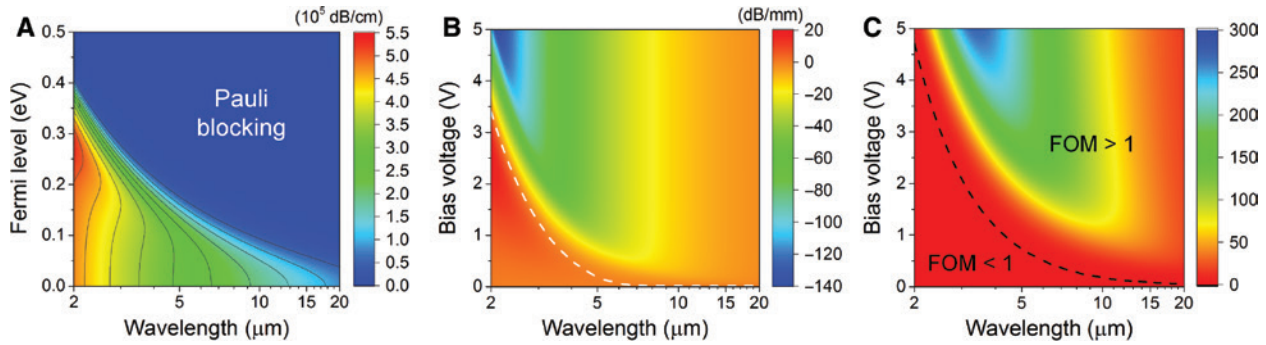
Figure 12: Performance projection for mid-IR graphene electroabsorption modulators.
(A) Contour plot showing the Fermi-level-dependent optical absorption of a graphene monolayer across the mid-IR band calculated using the surface conductive model; (B) simulated modulation depth of graphene mid-IR electroabsorption modulators, the white dashed line corresponds to zero modulation depth; (C) FOM (modulation depth/insertion loss) of the modulator: the black dashed line corresponds to unity FOM.

relative to the Dirac point.[2] The zero-absorption region in the upper right corner of the plot is a signature of Pauli blocking. To project the graphene modulator performance, a modulator configuration similar to that in Figure 11A is assumed. Other assumptions include the following: (1) starting Fermi level of graphene at zero bias coincides with the Dirac point, (2) a 20-nm layer of AMTIR-6 (As_2S_3) chalcogenide glass (dielectric constant 8.1 [167]) is chosen as the gate material given its considerably wider transparency window in the mid-IR compared to conventional oxide gates, and (3) confinement factor Γ of the waveguide mode in the graphene layers scales with wavelength as $1/\lambda$ and is quantitatively given by $\Gamma = 0.0034/\lambda$ (in μm).[3] The simulated modulation depth and electroabsorption modulation FOM (defined as the ratio of modulation depth to insertion loss) are plotted in Figure 12B and C, respectively. Two trends are evident: (1) higher bias voltage is needed for modulators operating at shorter wavelengths, as larger Femi level detuning is necessary to trigger Pauli blocking, and (2) both modulation depth and FOM reduce with increasing wavelength. At $\lambda > 10$ μm, the modulation depth drops to less than 10 dB/mm and plummets to 2.6 dB/mm at $\lambda = 20$ μm due to decreasing modal confinement in the graphene monolayer. To compensate for the diminishing modulation depth, long-wave infrared graphene modulators inevitably demand either large device footprint, which becomes impractical at $\lambda > 10$ μm, or multi-layer

graphene structures to augment spatial overlap with the optical mode.

4.5 Summary and outlook

As discussed above, choices abound for mid-IR on-chip modulation, and each technology has its pros and cons with respect to specific application scenarios. Our scaling analysis reveals a noteworthy trend; for most of these modulator technologies (thermo-optic, Pockels, free-carrier electro-optic, and graphene electroabsorption), their key performance metrics degrade towards longer wavelengths. This is an important consideration for modulator designs in the mid-IR. The only exception is free-carrier-based electroabsorption modulator, as FCA becomes more intense with increasing wavelength (before saturation occurs). We anticipate that it will become a powerful technology for light manipulation in the long-wave infrared.

5 Waveguide-integrated photodetectors

Photodetectors transform optical signals to the electronic realm and constitute an indispensable component of an integrated photonic circuit. Device fundamentals as well as latest progress of free-space mid-IR detectors and focal plane arrays (FPAs) have been summarized in several monographs and review articles [168–171]. In this section, we focus instead on waveguide-integrated mid-IR detector technologies.

---

2 In Figure 12A, a graphene monolayer thickness of 0.34 nm is assumed to obtain a finite effective absorption value.
3 The confinement factor is calculated for a TE-mode waveguide operating near single-mode cut-off (i.e. onset of the 2nd order TE mode). The waveguide dimensions scale linearly with wavelength to maintain single-mode operation.

Table 5: Mid-IR waveguide-integrated photodetectors on Si.

Type	Active material	Wavelength (µm)	Responsivity (A/W)	3 dB Bandwidth (GHz)	Room temperature NEP (pW/Hz$^{1/2}$)[a]	Reference
Heterogeneous integrated semiconductors	GaInAsSb on GaSb	2.3	1.4	N/A	0.54	[173–175]
	MQW on InP	2.35	1.6	N/A	0.035	[176, 177]
	InAsSb on GaSb	3.8	0.3	N/A	56	[178]
Monolithically integrated semiconductors	PbTe	2.1–2.5	1.0	N/A	0.69	[179]
2-D Van der Waals materials	Graphene/Si junction	2.75	0.13	N/A	0.36[b]	[180]
	Graphene	2.05	0.25	N/A	99	[142]
Ion-implanted silicon	Si$^+$ implanted Si	2.2–2.3	0.01	1.7	12.7[c]	[181]
	Zn$^+$ implanted Si	2.2–2.4	0.09	N/A	11.2	[182]
	Ar$^+$ implanted Si	2.2–2.3	0.021	N/A	2.2	[183]
	B$^+$ implanted Si	1.96–2.5	0.3	15	165	[184]
	S$^+$ implanted Si	3.36–3.74	0.0022	N/A	1000	[185]

[a]In a photoconductor or a zero-bias photodiode, the primary noise source is Johnson noise which is calculated from electrical resistance of the device. In a biased photodiode, shot noise usually dominates and it can be inferred from the dark current.
[b]A Fano factor of 1/3 is assumed in calculating shot noise in the graphene-based device.
[c]In the ion-implanted Si detectors, the quoted metrics (responsivity, bandwidth, and NEP) are often measured on different devices due to apparent large performance deviations (especially dark current) among devices. The best values for each metric are listed in the table.

In addition to the apparent advantage of facilitating on-chip integration, waveguide integration also introduces several important performance benefits. First, waveguide integration contributes to improved SNR by suppressing noise. This is because several types of noise (shot noise, Johnson noise, and generation-recombination noise) that often limit detector SNR linearly scale with the active volume of a detector [168]. When light is funneled into the detector via a waveguide (with core index n) rather than from free space, the detector active volume and hence noise can be reduced approximately by a factor of n^2 without compromising optical absorption. Such noise mitigation is critical in mid-IR detectors made of narrow-gap semiconductors, which suffer from a much higher noise floor. Second, waveguide-integrated detectors can achieve larger bandwidth than their free-space counterpart, as illustrated by Ahn [172]. Simply put, the smaller detector volume diminishes RC delay and carrier transit time in photovoltaic detectors. Last but not the least, waveguide-integrated detectors are not limited by the trade-off between optical absorption and charge carrier collection prevalent in free-space detectors [172]. High quantum efficiency requires a sufficiently large optical path length for complete absorption of incident photons, whereas efficient carrier collection requires a short carrier transit path to enhance quantum efficiency and transit-time-limited bandwidth in photovoltaic detectors or to boost photoconductive gain in photoconductors. Unlike free-space detectors where the optical path and

carrier collection path often coincide, the two paths are orthogonal in waveguide-integrated detectors, thereby circumventing the trade-off.

In the mid-IR spectral domain, four classes of waveguide-integrated detectors have been demonstrated, where the active detector material comprises (1) hybrid bonded narrow-gap semiconductors, (2) monolithically deposited or grown narrow-gap semiconductors, (3) narrow-gap Van der Waals semiconductors or semi-metals, or (4) ion-implanted Si with intentionally introduced gap states. Table 5 compares mid-IR waveguide-integrated detectors based on these technologies. Importantly, the SNR metric we opt for here is noise equivalent power (NEP) instead of specific detectivity (D⋆). In contrast to free-space detectors whose SNR scales with the square root of detector area, in waveguide-integrated detectors, the optical signal is channeled to the detector via a waveguide and therefore the square root scaling with detector area (which underlies the D⋆ definition) no longer holds.

The technologies used for fabricating the hybrid integrated detectors are similar to those applied to laser heterogeneous integration. As can be seen from Table 5, heterogeneously integrated III–V detectors claim the best performance in terms of both responsivity and SNR by virtue of the high semiconductor material quality. They are the rational choice when performance alone is the prime concern in designing a photonic system.

Unlike lasers, which mandate materials with a direct band gap, a small Auger rate constant, and minimal defect

density to inhibit non-radiative recombination, photodetectors place much less stringent requirements on the active materials. This is especially the case for waveguide-integrated detectors, whose small dimensions facilitate efficient carrier collection and noise suppression. Therefore, monolithic waveguide-integrated detectors can offer highly competitive performance despite the less than perfect material quality accessible to monolithic devices on Si, with the added advantage of significantly simplified integration process. In particular, polycrystalline lead salts represent an attractive option for monolithic on-chip mid-IR detector integration up to 5 μm. They can be deposited on Si in a non-epitaxial manner via thermal evaporation or solution processing [186–188]. They also epitomize a class of semiconductors whose polycrystalline form rivals or even outperforms their single crystalline counterparts for IR detection, a unique feature owing to spatial separation of charge carriers near grain boundaries and hence long photo-carrier lifetime [189, 190]. As an example, Figure 13 illustrates a PbTe detector integrated with a $Ge_{23}Sb_7S_{70}$ ChG waveguide [179]. The entire waveguide-detector structure is deposited and fabricated at low temperatures (<200°C) using a simple lithography and lift-off process compatible with CMOS-backend integration [191]. Monolithic integration of PbTe detector arrays with CMOS readout integrated circuits (ROICs) has also been demonstrated [192]. In addition to lead salts, other promising material candidates for monolithic mid-IR detection include GeSn [193] and colloidal quantum dots [194].

A second monolithic detector integration approach builds on Si itself. While crystalline Si has a band gap energy of 1.12 eV and is transparent in the mid-IR, mid-gap states that are optically absorbing in the mid-IR can be introduced either by substitutional doping or by forming lattice defects. Cryogenically cooled extrinsic Si and Ge detectors capitalizing on electronic transitions from shallow impurity dopant states to the conduction or valence band, in particular, blocked impurity band (BIB) detectors, are already pervasive for mid- and far-IR sensing [171]. Room-temperature operation of Zn and S ion implanted SOI detectors has been achieved, taking advantage of the relatively deep levels associated with the Zn and S dopants [182, 185]. Figure 14 illustrates the basic geometry and spectral response of a Zn-implanted p-i-n detector device seamlessly embedded in an SOI waveguide. Ion implantation also creates lattice defects with optically active trap states such as divacancies, and Si^+ and Ar^+ implanted SOI waveguide detectors belong to this category [181, 183]. These detectors are fully compatible with standard CMOS fabrication and do not necessitate the introduction of foreign materials in the
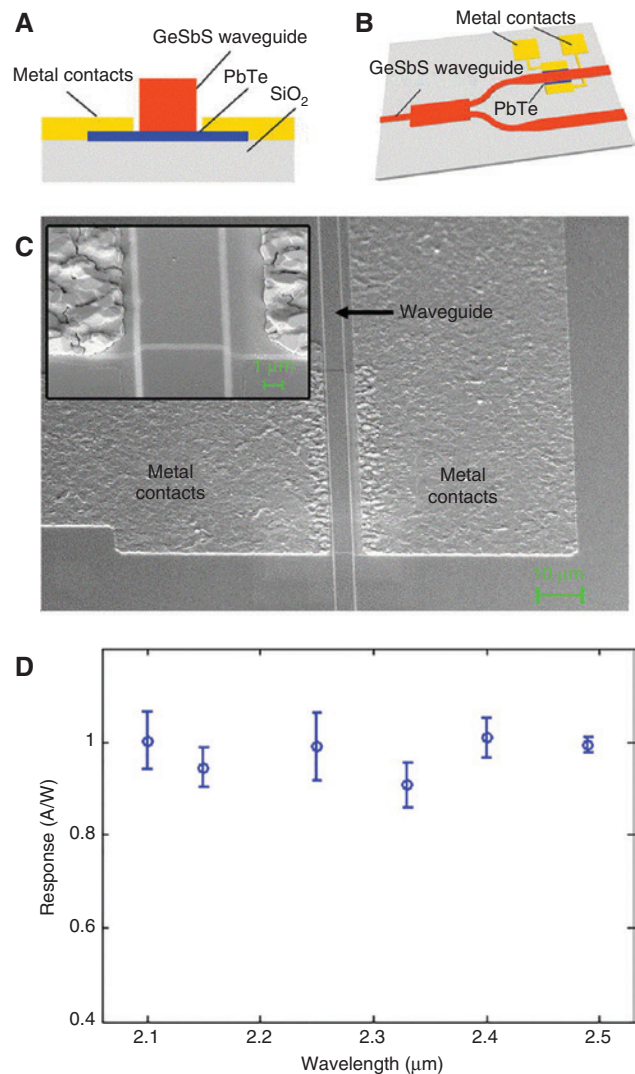

Figure 13: Mid-IR waveguide-integrated PbTe photodetector. (A, B) Schematic structure of the waveguide-integrated PbTe detector on Si, (C) tilted-view SEM image of the device, (D) measured responsivity of the detector showing a flat spectral response between 2.1- and 2.5-μm wavelength [179] (© 2016 AIP Publishing LLC).

Si platform. The main disadvantage of these detectors is their low responsivity due to the weak extrinsic dopant or defect level mediated absorption. Driving the device at high bias voltage in an avalanche mode markedly boosts its photoresponse albeit with the penalty of deteriorated noise figures [184]. Hyperdoping of Si with chalcogens via pulsed laser melting introduces strong sub-band gap absorption, although the prospect of efficient room-temperature mid-IR detection is ambiguous given the excessive dark current and noise in hyperdoped Si [195, 196].

Emerging two dimensional (2-D) Van der Waals crystals present another solution for mid-IR detection on Si. With its zero-gap nature, graphene exhibits broadband
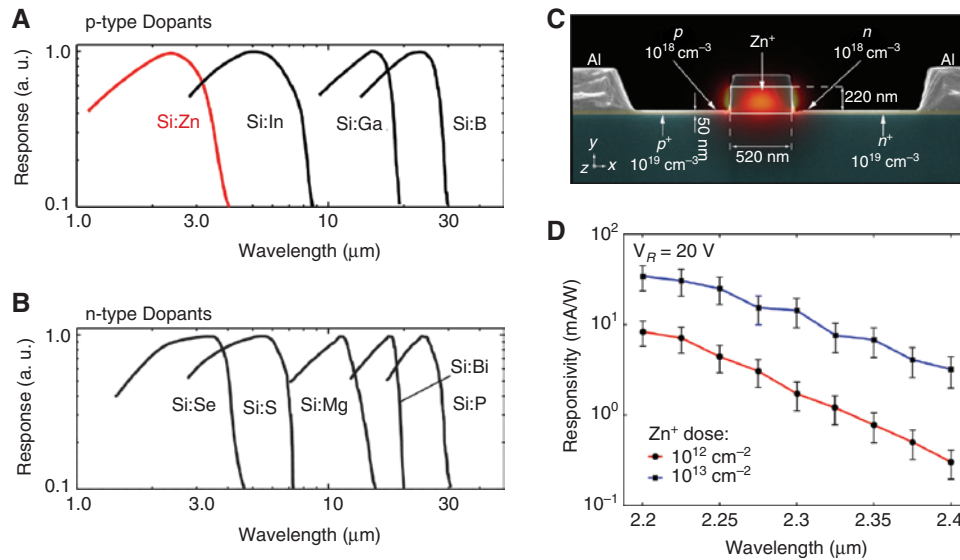
Figure 14: Extrinsic silicon for mid-IR detection.
(A, B) Normalized spectral response of bulk extrinsic silicon photoconductors for (A) p-type and (B) n-type dopants; (C) false color cross-sectional SEM image of a Zn-implanted SOI detector with TE mode intensity at 2.3 μm superimposed, photoelectrons generated through Zn dopant level absorption are collected by the lateral p-i-n diode structure; (D) spectral response of the detector [182] (© 2014 Optical Society of America).

absorption spanning the mid-IR spectrum. The lack of a band gap also results in a large dark current, short carrier lifetime, and poor detector NEP. The shortcoming can be mitigated by mating graphene with semiconductors to form a heterojunction [180] or replacing graphene with narrow-gap 2-D semiconductors such as BP [197], black arsenic phosphorus [198, 199], and tellurene [200]. To date, metal-catalyst-free, large-area growth of these 2-D materials on Si or dielectric substrates remains a significant technical barrier, and therefore, integration of these materials must resort to hybrid transfer processes. The promise of applying these materials to mid-IR photonics thus hinges on either successful incorporation of hybrid transfer into a standard CMOS-backend process or development of novel 2-D material monolithic integration techniques on Si.

Besides the direct detection methods described above, an indirect mid-IR detection scheme leverages nonlinear frequency up-conversion. In this approach, incident mid-IR radiation and pump light co-propagate in a nonlinear waveguide to generate an idler wave in the near-IR via FWM, and the idler wave is subsequently monitored using a near-IR detector. It has been theoretically shown that the indirect detection method can afford improved SNR under appropriate conditions, as near-IR detectors normally exhibit much higher SNR compared to mid-IR detectors [201, 202], and such mid-to-near-IR spectral translation (from 2.44 μm to 1.62 μm) was experimentally validated in SOI waveguides [202]. The need for a high-power pulsed pump source to enable efficient

wavelength conversion, however, poses a challenge towards on-chip integration.

6 On-chip waveguide spectrometers

A spectrometer is a device used to measure the spectrum of a polychromatic input, and it plays a crucial role in applications including spectroscopic sensing, laser wavelength monitoring, and hyperspectral imaging. On-chip waveguide spectrometers, where the optical input is fed into the spectrometer via an on-chip waveguide, potentially boast significant SWaP, robustness, and cost advantages over their traditional counterparts assembled from bulk optics.

A variety of on-chip spectrometer designs have been unveiled over the past decade, either in the "dispersive" configuration or following the "modulated" scheme [203]. In the former type of devices, the spectral components of the incident light are spatially split to form a spectrograph, which is then recorded by a detector array to decode the spectral information. This type of spectrometer includes wavelength (de)multiplexers such as arrayed waveguide gratings (AWG), planar concave gratings (PCG), and micro-resonator arrays. It also encompasses those operating on the wavelength multiplexing principle such as spatial heterodyne

Table 6: Mid-IR on-chip waveguide spectrometers; specifications of a COTS portable spectrometer (Ocean Optics NIRQuest512-2.5) are also listed for comparison.

Material platform	Device type	Center wavelength (µm)	Bandwidth (nm)	Spectral resolution (nm)	Number of spectral channels N	Footprint (mm²)	Insertion loss (dB)[a]	Reference
	NIRQuest512-2.5	1.7	1600	3.125 (10 µm slit)	512	940 cm³	N/A	[205]
SOI	AWG	3.8	60	9.6	6	0.75	1.5−2	[178, 206]
	PCG		80	10	8	3.06	1.5−3	
SOI	AWG	2.2	10	1.6	6	1.0	4	[175]
	PCG	2.125	100	6	16	0.54	5	
SOI	AWG	2.375	50	4.2	12	0.64	3	[176]
SOI	Interleaved angled MMI	3.76	80	13	6	N/A	3−4	[207]
SOI	SHS	3.75	59	2.7	21	95	N/A	[204]
Ge-on-Si	AWG	5.35	90	18	5	1.0	2.5−3	[25]
Ge-on-Si	PCG	5.25	150	25	6	1.8	4−5	[26]
Graded SiGe	AWG	4.48	90	5.9	15	200	3−5	[208]
Graded SiGe	AWG	7.6	580	17	35	N/A	3	[209]

[a]Here we only take into account insertion loss of the spectral splitting devices and do not include losses due to fiber-to-waveguide coupling or coupling to photodetectors.

spectrometer (SHS) [204]. To the best of the authors' knowledge, all on-chip mid-IR waveguide spectrometers demonstrated hitherto belong to this category (Table 6). Despite their conceptual simplicity, on-chip dispersive type spectrometers are confronted with two main limitations. One is the fundamental trade-off between spectral resolution and signal throughput (and hence SNR), as refining the resolution requires splitting the signal into more spatial channels. The other more severe challenge is scaling; as can be seen from Table 6, there is a vast gap between the number of spectral channels N (which approximately equals spectral bandwidth divided by resolution) afforded by an on-chip spectrometer and a COTS product. In the dispersive spectrometer designs named above, the device footprint roughly scales with N linearly. Moreover, the number of photodetectors and electrical leads also scales with N. The linear scaling law precludes current on-chip spectrometers from reaching the level of performance furnished by a laboratory-grade instrument as a consequence of the unsustainable complexity escalation.

On the other hand, Fourier transform infrared (FTIR) spectrometers epitomize the "modulated" type devices. In these spectrometers, the device is cyclically modulated to generate a set of linearly independent transmittance states, and the resulting total transmitted intensity is monitored using one or two single-element detectors. A Fourier transform (or a linear transform in the general case) connects the time-varying signal recorded by the detector(s) and the spectrum of the incident light [203]. Unlike the dispersive spectrometers, the "modulated" spectrometers are not bound by the trade-off between spectral resolution and SNR, a feature known as the Fellgett's advantage. On-chip FTIR spectrometers have been realized in the near-IR based on MZIs with a thermo-optically or electro-optically tunable arm [210, 211], although the small phase shift accessible through the thermo-optic or electro-optic modulation seriously limits their spectral resolution.

Here we describe a digital Fourier transform infrared (dFTIR) spectrometer design to resolve the aforementioned challenges [203]. The device design is depicted in the block diagram in Figure 15A. The device consists of an MZI whose arms comprise a series of cascaded optical switches connected by waveguides of varying lengths. The optical paths in the interferometer arms are modified by routing light through different waveguide branches via the switches. When light travels through the reference paths (marked with orange color) in both MZI arms, the MZI is balanced and the path length difference between the two arms is zero. Each path in red is different from the reference paths by a power of two times ΔL (ΔL being a pre-defined path length difference). According to this design, each permutation of the optical switches results in a different difference in optical path length between the two arms, covering 0, ΔL, $2\Delta L$, $4\Delta L$... to $(2^j - 1) \cdot \Delta L$, where j is the total number of optical switches. The design thereby offers a spectral channel number of:
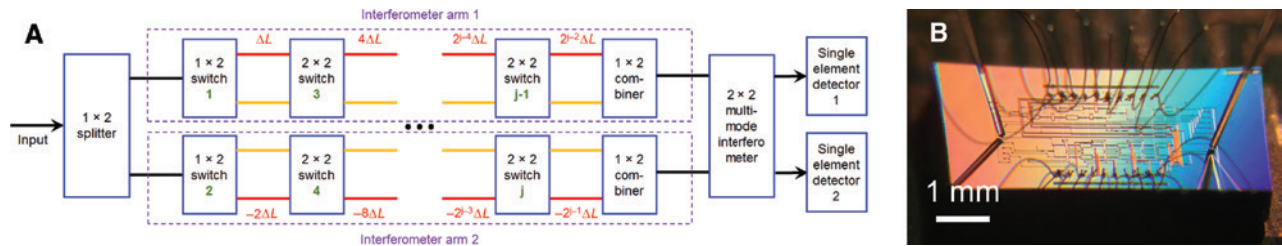
$$N = 2^j. \tag{6}$$

Figure 15: dFTIR spectrometer.
(A) Block diagram illustrating the dFTIR spectrometer layout [203] (© 2017 IEEE), (B) a photo of a dFTIR chip.

The spectral resolution $\delta\lambda$ and the bandwidth BW are given by:

$$\delta\lambda = \frac{1}{2^j} \cdot \frac{\lambda^2}{n_{\text{eff}} \cdot \Delta L}, \tag{7}$$

and

$$BW = N \cdot \delta\lambda = \frac{\lambda^2}{n_{\text{eff}} \cdot \Delta L}. \tag{8}$$

A salient feature of the dFTIR spectrometer is its exponential scaling behavior for both spectral channel number and resolution. A second benefit of the dFTIR design is that it only needs one or two single-element detectors rather than a detector array, which leads to significant cost savings and drastically simplified system design, processing, and packaging. Our analysis concludes that with 12 switches, a near-IR dFTIR device can claim an unprecedented spectral channel number of 4096, a fine resolution down to 0.02 nm, a moderate insertion loss of less than 6 dB, and a small footprint that fits into a millimeter-sized chip [203]. Figure 15B shows the photo of a 64-channel dFTIR spectrometer prototyped through a commercial multi-project-wafer (MPW) process operating across the C-band with a spectral resolution of 0.5 nm. The design can readily be scaled to the mid-IR

band, building on the component technologies discussed in previous sections.

7 A case in point for mid-IR photonic integration: spectroscopic sensor-on-a-chip

In this section, we seek to construct a hypothetical on-chip sensor based on component technologies discussed in preceding sections as an example of mid-IR photonic integration. The sensor is designed to identify and quantify hydrocarbon chemicals in a multi-component gaseous analyte using a fully integrated, chip-scale system. To meet the demands of both detection sensitivity and selectivity, we define the operational wavelength range to be 3–3.8 μm, which encompasses the primary absorption bands of hydrocarbons. Figure 16 depicts a schematic layout of the envisioned sensor-on-a-chip module consisting of an on-chip source, a sensing element where light interacts with the analyte, and a light analysis unit that processes the transmitted signal to generate an optical spectrum containing quantitative information on the analyte chemical composition. In the following, we elaborate our rationale for component
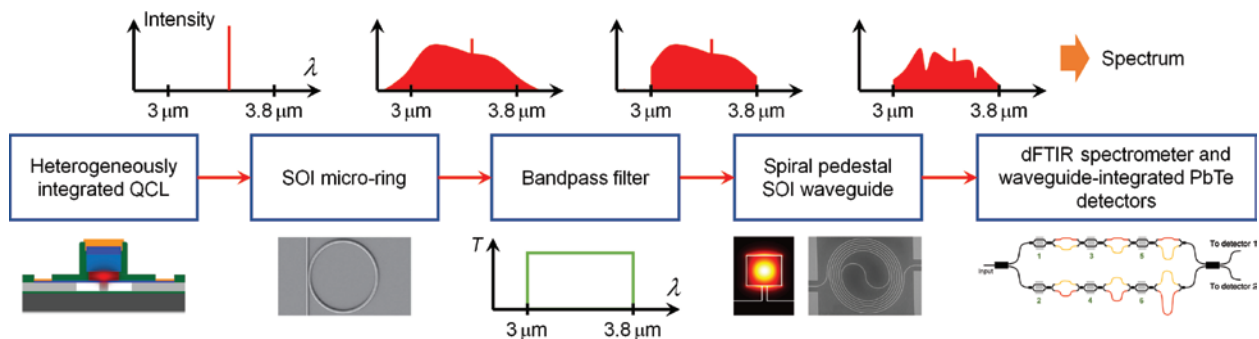

Figure 16: A hypothetical sensor-on-a-chip system for spectroscopic sensing across the 3–3.8-μm band; the sensor is designed for hydrocarbon gas sensing in a chemically cluttered environment and all of its components are integrated on-chip.

choices and provide a quantitative performance projection of the sensing system.

7.1 Component selection

We choose a micro-resonator FC pumped by a heterogeneously integrated DFB QCL as the light source, because it is the only option that meets both on-chip integration and broadband coverage requirements. Figure 6 gives an example of a FC covering the entire 3–3.8 μm [105], which we use here as the basis for our calculation. Mode-locking the FC to a single soliton state ensures a low-noise comb spectrum essential for spectroscopic interrogation [108]. We note that the FC is pumped at 3.07 μm, a wavelength difficult to access with existing QCL technologies. However, with appropriate dispersion engineering, the micro-resonator can also be pumped at slightly longer wavelengths (e.g. 3.5 μm) while maintaining the same spectral coverage. The FC shown in Figure 6 is produced with a pump power of 80 mW, within the reach of current DFB QCL integration technology [73]. The heterogeneously integrated QCL emits into the transverse magnetic (TM) mode, which further benefits the sensing application due to the stronger evanescent fields.

The sensing element can assume the form of a micro-resonator [212] or a spiral waveguide [62]. In both cases, the analyte molecules interact with the evanescent field of the guided optical mode, and the detection sensitivity is ultimately bound by propagation loss of the waveguide. Considering a spiral waveguide with length L and loss α (in the absence of optically absorbing analytes), fractional change of transmitted light intensity $\Delta I\%$ imposed by analyte absorption is given by:

$$\Delta I\% = \exp(-\alpha L) \cdot [1 - \exp(-\Gamma \alpha' L)] \approx \exp(-\alpha L) \cdot \Gamma \alpha' L, \quad (9)$$

where α' denotes the absorption coefficient of the analyte and Γ is the modal confinement factor in the gas-phase analyte. The waveguide length conducive to optimum sensitivity must yield the maximum detectable optical attenuation $\Delta I\%$, i.e.:

$$\frac{\partial(\Delta I\%)}{\partial L} = 0 \Rightarrow L = \frac{1}{\alpha}. \quad (10)$$

Therefore, the waveguide should support low-loss propagation within the target spectral band. The onset of phonon absorption in SiO_2 sets a lower bound of propagation loss at ~0.3 dB/cm for an air-clad SOI waveguide (Figure 2). The loss bound can be further reduced by an oxide undercut etch, which at the same time enhances the evanescent wave confinement in the surrounding gas phase. Here we assume an oxide-pedestal Si waveguide with a core size of 1 μm by 1 μm. The waveguide dimensions are chosen to guarantee single-mode operation from 3 to 3.8 μm. The simulated TM mode confinement factors in the gas phase and in the oxide pedestal are 10% (averaged over 3–3.8 μm) and 1.8% (at 3.8 μm), respectively, and the latter indicates a negligible loss ceiling of 0.1 dB/cm due to oxide absorption. We therefore assume an SOI waveguide loss of 0.2 dB/cm based on literature values [9] and a spiral length $L = 21.7$ cm according to Eq. (10).

An on-chip spectrometer is employed to acquire the absorption spectrum. The comb line spacing is 127 GHz, corresponding to a total of 166 comb lines between 3 and 3.8 μm. A dFTIR spectrometer with eight switches (affording a maximum of 256 spectral channels) readily resolves the comb spectrum (with oversampling), and the large thermo-optic coefficient of Si facilitates efficient optical switching in the dFTIR spectrometer. It is worth noting that while the 3–3.8-μm band exceeds the bandwidth of most on-chip switches, spectral information can nonetheless be inferred using the dFTIR spectrometer from a generic linear transform with a pre-calibrated transformation matrix [203].

Among the detector materials listed in Table 5, InAsSb, PbTe, graphene, and S^+-implanted Si cover the target spectral range. We select PbTe given its superior SNR and ease of integration with the SOI platform.

7.2 Performance projection

Limit of detection (LOD) is projected based on SNR of the sensor. According to Figure 6, we take a conservative estimate of –30 dBm or 1-μW power of each comb line in the 3–3.8-μm range. Optical power from each comb line reaching the detector is 0.18 μW after taking into account the insertion losses of all components (spiral waveguide: 4.3 dB; spectrometer: 3.2 dB [203]). We first estimate the noise contribution from the PbTe detector. Given an NEP of 0.69 pW/Hz$^{1/2}$ and a factor of $\sqrt{166/2} = 6.4$ SNR enhancement from the Fellgett's advantage [213], the detector-limited noise-equivalent absorbance (NEA, given as the minimum detectable absorbance $\Gamma \alpha' L$) is NEP/(0.18 μW)/6.4 = 6.0×10^{-7} Hz$^{-1/2}$. Such an impressive NEA, while quoted in previous on-chip sensor performance projections [214], is challenging to attain in practice [215]. Empirically, NEA down to 8.5×10^{-4} Hz$^{-1/2}$ has been experimentally measured in on-chip waveguide sensors [216]. For hydrocarbons, their peak absorption cross-sections at 3–3.8 μm are typically about 10^{-18} cm^2, equivalent to

an absorption coefficient of 27 cm^{-1} in pure gases [217]. Taking the NEA value of 8.5×10^{-4} Hz$^{-1/2}$, the LOD is therefore 14.5 ppmv Hz$^{-1/2}$, which represents over two orders of magnitude improvement compared to state-of-the-art on-chip sensors operating in the near-IR [216]. With 10-s integration time, the sensor can detect hydrocarbons down to 3.2 ppmv. Further sensitivity boost into the ppbv regime mandates new detection schemes that can transcend the optical path length limit, for example, through cavity-enhanced photothermal spectroscopy [218–220].

Next, we analyze the power consumed by the sensor. Current heterogeneously integrated QCLs have wall plug efficiencies around 0.5%. To maintain an 80-mW output, 16-W driving power is needed, which dwarfs the power consumption of other components. For instance, state-of-the-art telecom-band thermo-optic switches feature a phase-shifting efficiency of 2 mW/π [143]. Even after accounting for the λ^3 scaling, the dFTIR spectrometer merely consumes 0.08-W average power, which can be further reduced by improving thermal isolation of phase shifters in the switches.

Last, we estimate the footprint of the sensor. A previously demonstrated hybrid DFB QCL has a gain region of 3 mm in length [73]. Given its high index contrast, the pedestal SOI waveguide permits low-loss bends with radii below 20 μm and a waveguide spacing of 5.3 μm. Thus the spiral waveguide (with a total length of 21.7 cm) fills an area of less than 1 mm^2. The total dFTIR spectrometer length is estimated following previously described protocols [203] to be 1.8 mm. The areas occupied by the microring and the filter are negligible compared to the other components. In total, the entire circuit can readily fit into a chip of 1×6 mm^2 in size.

In summary, we show that the sensor-on-a-chip system features ppmv-level, multi-species quantification capability within a small footprint of <6 mm^2. However, significant improvements are needed to reduce its excessive power consumption currently limited by the low wall plug efficiency of heterogeneously integrated mid-IR lasers.

8 Summary

As we draw a conclusion to this article, it is worth highlighting that most examples cited here, which are selected from the large body of work referenced in this review, took place in the last 5 years. This is a clear indication that the mid-IR represents a new frontier for photonic integration on Si.

Despite the significant strides over the past few years, many challenges await because of both the less mature device technologies compared to their near-IR counterparts and the fundamental limitations as a consequence of wavelength scaling. Multi-material integration beyond the traditional silicon-based material repertoire, which has been a key driver for advances in this field, will continue to play a vital role in addressing the challenges.

In addition, transitioning from optimization of individual photonic devices to system-level integration bears major opportunities for mid-IR photonics. As our sensor-on-a-chip example illustrates, full-fledged, chip-scale mid-IR photonic systems with performances well exceeding state-of-the-art are already reasonably within the reach of existing technologies. We foresee that such integrated mid-IR photonic modules will turn into reality as photonic manufacturing strives to embrace new materials and integration technologies in the next decade.

References

[1] Pile D, Horiuchi N, Won R, Graydon O. Extending opportunities. Nat Photonics 2012;6:407.

[2] Soref RA, Emelett SJ, Buchwald WR. Silicon waveguided components for the long-wave infrared region. J Optics A Pure Appl Optics 2006;8:840.

[3] Hu J, Meyer J, Richardson K, Shah L. Feature issue introduction: mid-IR photonic materials. Opt Mater Express 2013;3:1571–5.

[4] Soref R. Mid-infrared photonics in silicon and germanium. Nat Photonics 2010;4:495–7.

[5] Mashanovich GZ, Milošević MM, Nedeljkovic M, et al. Low loss silicon waveguides for the mid-infrared. Opt Express 2011;19:7112–9.

[6] Lin PT, Singh V, Lin HY, Tiwald T, Kimerling LC, Agarwal AM. Low-stress silicon nitride platform for mid-infrared broadband and monolithically integrated microphotonics. Adv Opt Mater 2013;1:732–9.

[7] Kitamura R, Pilon L, Jonasz M. Optical constants of silica glass from extreme ultraviolet to far infrared at near room temperature. Appl Opt 2007;46:8118–33.

[8] Milošević MM, Nedeljkovic M, Ben Masaud TM, et al. Silicon waveguides and devices for the mid-infrared. Appl Phys Lett 2012;101:121105.

[9] Miller SA, Yu M, Ji X, et al. Low-loss silicon platform for broadband mid-infrared photonics. Optica 2017;4:707–12.

[10] Khan S, Chiles J, Ma J, Fathpour S. Silicon-on-nitride waveguides for mid- and near-infrared integrated photonics. Appl Phys Lett 2013;102:121104.

[11] Singh V, Lin PT, Patel N, et al. Mid-infrared materials and devices on a Si platform for optical sensing. Sci Technol Adv Mater 2014;15:014603.

[12] Xia Y, Qiu C, Zhang X, Gao W, Shu J, Xu Q. Suspended Si ring resonator for mid-IR application. Opt Lett 2013;38:1122–4.

[13] Shankar R, Leijssen R, Bulu I, Loncar M. Mid-infrared photonic crystal cavities in silicon. Opt Express 2011;19:5579–86.

[14] Penades JS, Ortega-Moñux A, Nedeljkovic M, et al. Suspended silicon mid-infrared waveguide devices with subwavelength grating metamaterial cladding. Opt Express 2016;24:22908–16.

[15] Nedeljkovic M, Penadés JS, Mitchell CJ, et al. Surface-grating-coupled low-loss Ge-on-Si Rib waveguides and multimode interferometers. IEEE Photonics Technol Lett 2015;27:1040–3.

[16] Lin HT, Li L, Zou Y, et al. Demonstration of high-Q mid-infrared chalcogenide glass-on-silicon resonators. Opt Lett 2013;38:1470–2.

[17] Li W, Anantha P, Bao S, et al. Germanium-on-silicon nitride waveguides for mid-infrared integrated photonics. Appl Phys Lett 2016;109:241101.

[18] Lin PT, Singh V, Cai Y, Kimerling LC, Agarwal A. Air-clad silicon pedestal structures for broadband mid-infrared microphotonics. Opt Lett 2013;38:1031–3.

[19] Lin PT, Singh V, Wang J, et al. Si-CMOS compatible materials and devices for mid-IR microphotonics. Opt Mater Express 2013;3:1474–87.

[20] Cheng ZZ, Chen X, Wong CY, Xu K, Tsang HK. Mid-infrared suspended membrane waveguide and ring resonator on silicon-on-insulator. IEEE Photonics J 2012;4:1510–9.

[21] Chiles J, Khan S, Ma J, Fathpour S. High-contrast, all-silicon waveguiding platform for ultra-broadband mid-infrared photonics. Appl Phys Lett 2013;103:151106.

[22] Chiles J, Fathpour S. Single-mode and single-polarization photonics with anchored-membrane waveguides. Opt Express 2016;24:19337–43.

[23] Penades JS, Alonso-Ramos C, Khokhar AZ, et al. Suspended SOI waveguide with sub-wavelength grating cladding for mid-infrared. Opt Lett 2014;39:5661–4.

[24] Chang YC, Paeder V, Hvozdara L, Hartmann JM, Herzig HP. Low-loss germanium strip waveguides on silicon for the mid-infrared. Opt Lett 2012;37:2883–5.

[25] Malik A, Muneeb M, Pathak S, et al. Germanium-on-silicon mid-infrared arrayed waveguide grating multiplexers. IEEE Photonics Technol Lett 2013;25:1805–8.

[26] Malik A, Muneeb M, Shimura Y, Van Campenhout J, Loo R, Roelkens G. Germanium-on-silicon planar concave grating wavelength (de)multiplexers in the mid-infrared. Appl Phys Lett 2013;103:161119.

[27] Mashanovich GZ, Mitchell CJ, Penades JS, et al. Germanium mid-infrared photonic devices. J Lightwave Technol 2017;35:624–30.

[28] Alonso-Ramos C, Nedeljkovic M, Benedikovic D, et al. Germanium-on-silicon mid-infrared grating couplers with low-reflectivity inverse taper excitation. Opt Lett 2016;41:4324–7.

[29] Kang J, Cheng Z, Zhou W, et al. Focusing subwavelength grating coupler for mid-infrared suspended membrane germanium waveguides. Opt Lett 2017;42:2094–7.

[30] Xiao T-H, Zhao Z, Zhou W, et al. Mid-infrared germanium photonic crystal cavity. Opt Lett 2017;42:2882–5.

[31] Mittal V, Sessions NP, Wilkinson JS, Murugan GS. Optical quality ZnSe films and low loss waveguides on Si substrates for mid-infrared applications. Opt Mater Express 2017;7:712–25.

[32] Hô N, Phillips MC, Qiao H, et al. Single-mode low-loss chalcogenide glass waveguides for the mid-infrared. Opt Lett 2006;31:1860–2.

[33] Ma P, Choi DY, Yu Y, et al. Low-loss chalcogenide waveguides for chemical sensing in the mid-infrared. Opt Express 2013;21:29927–37.

[34] Yu Y, Gai X, Ma P, et al. A broadband, quasi-continuous, mid-infrared supercontinuum generated in a chalcogenide glass waveguide. Laser Photonics Rev 2014;8:792–8.

[35] Ma P, Choi DY, Yu Y, et al. High Q factor chalcogenide ring resonators for cavity-enhanced MIR spectroscopic sensing. Opt Express 2015;23:19969–79.

[36] Gutierrez-Arroyo A, Baudet E, Bodiou L, et al. Optical characterization at 7.7 µm of an integrated platform based on chalcogenide waveguides for sensing applications in the mid-infrared. Opt Express 2016;24:23109–17.

[37] Baudet E, Gutierrez-Arroyo A, Baillieul M, et al. Development of an evanescent optical integrated sensor in the mid-infrared for detection of pollution in groundwater or seawater. Adv Device Mater 2017;3:1–7.

[38] Lewi T, Katzir A. Silver halide single-mode strip waveguides for the mid-infrared. Opt Lett 2012;37:2733–5.

[39] Morrison B, Casas-Bedoya A, Ren G, et al. Compact Brillouin devices through hybrid integration on silicon. Optica 2017;4:847–54.

[40] Reimer C, Nedeljkovic M, Stothard DJ, et al. Mid-infrared photonic crystal waveguides in silicon. Opt Express 2012;20:29361–8.

[41] Kuyken B, Ideguchi T, Holzner S, et al. An octave-spanning mid-infrared frequency comb generated in a silicon nanophotonic wire waveguide. Nat Commun 2015;6:6310.

[42] Penades JS, Khokhar AZ, Nedeljkovic M, Mashanovich GZ. Low-loss mid-infrared SOI slot waveguides. IEEE Photonics Technol Lett 2015;27:1197–9.

[43] Dong BW, Guo X, Ho CP, et al. Silicon-on-insulator waveguide devices for broadband mid-infrared photonics. IEEE Photonics J 2017;9. Article sequence number 4501410.

[44] Baehr-Jones T, Spott A, Ilic R, et al. Silicon-on-sapphire integrated waveguides for the mid-infrared. Opt Express 2010;18:12127–35.

[45] Spott A, Liu Y, Baehr-Jones T, Ilic R, Hochberg M. Silicon waveguides and ring resonators at 5.5 µm. Appl Phys Lett 2010;97:213501.

[46] Li FX, Jackson SD, Grillet C, et al. Low propagation loss silicon-on-sapphire waveguides for the mid-infrared. Opt Express 2011;19:15212–20.

[47] Wong CY, Cheng Z, Chen X, et al. Characterization of mid-infrared silicon-on-sapphire microring resonators with thermal tuning. IEEE Photonics J 2012;4.

[48] Shankar R, Bulu I, Loncar M. Integrated high-quality factor silicon-on-sapphire ring resonators for the mid-infrared. Appl Phys Lett 2013;102:051108.

[49] Zou Y, Subbaraman H, Chakravarty S, et al. Grating-coupled silicon-on-sapphire integrated slot waveguides operating at mid-infrared wavelengths. Opt Lett 2014;39:3070–3.

[50] Singh N, Casas-Bedoya A, Hudson DD, Read A, Mägi E, Eggleton BJ. Mid-IR absorption sensing of heavy water using a silicon-on-sapphire waveguide. Opt Lett 2016;41:5776–9.

[51] Zou Y, Chakravarty S, Wray P, Chen RT. Experimental demonstration of propagation characteristics of mid-infrared photonic crystal waveguides in silicon-on-sapphire. Opt Express 2015;23:6965–75.

[52] Carletti L, Sinobad M, Ma P, et al. Mid-infrared nonlinear optical response of Si-Ge waveguides with ultra-short optical pulses. Opt Express 2015;23:32202–14.

[53] Carletti L, Ma P, Yu Y, et al. Nonlinear optical response of low loss silicon germanium waveguides in the mid-infrared. Opt Express 2015;23:8261–71.

[54] Ettabib MA, Xu L, Bogris A, et al. Broadband telecom to mid-infrared supercontinuum generation in a dispersion-engineered silicon germanium waveguide. Opt Lett 2015;40:4118–21.

[55] Ramirez JM, Vakarin V, Frigerio J, et al. Ge-rich graded-index Si1-xGex waveguides with broadband tight mode confinement and flat anomalous dispersion for nonlinear midinfrared photonics. Opt Express 2017;25:6561–7.

[56] Ramirez JM, Vakarin V, Gilles C, et al. Low-loss Ge-rich Si0.2Ge0.8 waveguides for mid-infrared photonics. Opt Lett 2017;42:105–8.

[57] Kang J, Takenaka M, Takagi S. Novel Ge waveguide platform on Ge-oninsulator wafer for mid-infrared photonic integrated circuits. Opt Express 2016;24:1855–64.

[58] Lin PT, Singh V, Kimerling L, Agarwal AM. Planar silicon nitride mid-infrared devices. Appl Phys Lett 2013;102:251121.

[59] Lin PT, Giammarco J, Borodinov N, et al. Label-free water sensors using hybrid polymer-dielectric mid-infrared optical waveguides. ACS Appl Mater Interfaces 2015;7:11189–94.

[60] Luke K, Okawachi Y, Lamont MRE, Gaeta AL, Lipson M. Broadband mid-infrared frequency comb generation in a Si3N4 microresonator. Opt Lett 2015;40:4823–6.

[61] Gai X, Choi DY, Madden S, Yang Z, Wang R, Luther-Davies B. Supercontinuum generation in the mid-infrared from a dispersion-engineered As2S3 glass rib waveguide. Opt Lett 2012;37:3870–2.

[62] Han Z, Lin P, Singh V, et al. On-chip mid-infrared gas detection using chalcogenide glass waveguide. Appl Phys Lett 2016;108:141106.

[63] Lin PT, Jung H, Kimerling LC, Agarwal A, Tang HX. Low-loss aluminium nitride thin film for mid-infrared microphotonics. Laser Photonics Rev 2014;8:L23–8.

[64] Wang XF, Karlsson M, Forsberg P, et al. Diamonds are a spectroscopist's best friend: thin-film diamond mid-infrared waveguides for advanced chemical sensors/biosensors. Anal Chem 2014;86:8136–41.

[65] Malmstrom M, Karlsson M, Forsberg P, Cai Y, Nikolajeff F, Laurell F. Waveguides in polycrystalline diamond for mid-IR sensing. Opt Mater Express 2016;6:1286–95.

[66] Robinson JT, Preston K, Painter O, Lipson M, First-principle derivation of gain in high-index-contrast waveguides Opt Express 2008;16:16659–69.

[67] Cheng ZZ, Chen X, Wong CY, et al. Focusing subwavelength grating coupler for mid-infrared suspended membrane waveguide. Opt Lett 2012;37:1217–9.

[68] Radosavljevic S, Kuyken B, Roelkens G. Efficient 5.2 um wavelength fiber-to-chip grating couplers for the Ge-on-Si and Ge-on-SOI mid-infrared waveguide platform. Opt Express 2017;25:19034–42.

[69] Griffith AG, Lau RK, Cardenas J, et al. Silicon-chip mid-infrared frequency comb generation. Nat Commun 2015;6:6299.

[70] Yao Y, Hoffman AJ, Gmachl CF. Mid-infrared quantum cascade lasers. Nat Photonics 2012;6:432–9.

[71] Vurgaftman I, Weih R, Kamp M, et al. Interband cascade lasers. J Phys D: Appl Phys 2015;48:123001.

[72] Spott A, Peters J, Davenport ML, et al. Quantum cascade laser on silicon. Optica 2016;3:545–51.

[73] Spott A, Peters J, Davenport ML, et al. Heterogeneously integrated distributed feedback quantum cascade lasers on silicon. Photonics 2016;3:35.

[74] Veerabathran G, Sprengel S, Andrejew A, Amann M-C. Room-temperature vertical-cavity surface-emitting lasers at 4 μm with GaSb-based type-II quantum wells. Appl Phys Lett 2017;110:071104.

[75] Spott A, Davenport M, Peters J, et al. Heterogeneously integrated 2.0 μm CW hybrid silicon lasers at room temperature. Opt Lett 2015;40:1480–3.

[76] Wang R, Sprengel S, Boehm G, et al. 2.3 μm Range InP-based type-II quantum well Fabry-Perot lasers heterogeneously integrated on a silicon photonic integrated circuit. Opt Express 2016;24:21081–9.

[77] Wang R, Sprengel S, Malik A, et al. Heterogeneously integrated III−V-on-silicon 2.3×μm distributed feedback lasers based on a type-II active region. Appl Phys Lett 2016;109:221111.

[78] Roelkens G, Dave U, Gassenq A, et al. Silicon-based photonic integration beyond the telecommunication wavelength range. IEEE J Sel Topics Quantum Electron 2014;20:394–404.

[79] Volet N, Spott A, Stanton EJ, et al. Semiconductor optical amplifiers at 2.0-μm wavelength on silicon. Laser Photonics Rev 2017;11. Article number 1600165.

[80] Yariv A, Sun X. Supermode Si/III−V hybrid lasers, optical amplifiers and modulators: a proposal and analysis. Opt Express 2007;15:9147–51.

[81] Wang R, Malik A, Šimonytė I, Vizbaras A, Vizbaras K, Roelkens G. Compact GaSb/silicon-on-insulator 2.0×μm widely tunable external cavity lasers. Opt Express 2016;24:28977–86.

[82] Wang R, Sprengel S, Boehm G, Baets R, Amann MC, Roelkens G. Broad wavelength coverage 2.3 μm III-V-on-silicon DFB laser array. Optica 2017;4:972–5.

[83] Spott A, Stanton EJ, Volet N, Peters JD, Meyer JR, Bowers JE. Heterogeneous integration for mid-infrared silicon photonics. IEEE J Sel Topics Quantum Electron 2017;23. Article sequence number 8200810.

[84] Zhang L, Agarwal AM, Kimerling LC, Michel J. Nonlinear Group IV photonics based on silicon and germanium: from near-infrared to mid-infrared. Nanophotonics 2014;3:247–68.

[85] Jalali B, Raghunathan V, Dimitropoulos D, Boyraz O. Raman-based silicon photonics. IEEE J Sel Topics Quantum Electron 2006;12:412–21.

[86] Boyraz O, Jalali B. Demonstration of a silicon Raman laser. Opt Express 2004;12:5269–73.

[87] Rong H, Jones R, Liu A, Cohen O. A continuous-wave Raman silicon laser. Nature 2005;433:725.

[88] Rong H, Xu S, Cohen O, et al. A cascaded silicon Raman laser. Nat Photonics 2008;2:170–4.

[89] Raghunathan V, Borlaug D, Rice RR, Jalali B. Demonstration of a mid-infrared silicon Raman amplifier. Opt Express 2007;15:14355–62.

[90] Jalali B, Raghunathan V, Shori R, Fathpour S, Dimitropoulos D, Stafsudd O. Prospects for silicon mid-IR Raman lasers. IEEE J Sel Topics Quantum Electron 2006;12:1618–27.

[91] Passaro V, De Leonardis F. Investigation of SOI Raman lasers for mid-infrared gas sensing. Sensors 2009;9:7814–36.

[92] Zhang X, Feng M, Zhang X, Xu J. Mid-infrared light generation by high order SRS effect in silicon ring cavity. J Opt 2011;14:015201.

[93] Latawiec P, Venkataraman V, Burek MJ, Hausmann BJ, Bulu I, Loncar M. On-chip diamond Raman laser. Optica 2015;2:924–8.

[94] Zlatanovic S, Park JS, Moro S, et al. Mid-infrared wavelength conversion in silicon waveguides using ultracompact telecom-band-derived pump source. Nat Photonics 2010;4:561–4.

[95] Kuyken B, Liu X, Osgood RM, Baets R, Roelkens G, Green WM. A silicon-based widely tunable short-wave infrared optical parametric oscillator. Opt Express 2013;21:5931–40.

[96] Kuyken B, Verheyen P, Tannouri P, et al. Generation of 3.6 μm radiation and telecom-band amplification by four-wave mixing in a silicon waveguide with normal group velocity dispersion. Opt Lett 2014;39:1349–52.

[97] Kuyken B, Leo F, Mussot A, Kudlinski A, Roelkens G. A two-stage photonic crystal fiber/silicon photonic wire short-wave infrared wavelength converter/amplifier based on a 1064 nm pump source. Opt Express 2015;23:13025–31.

[98] Turner-Foster AC, Foster MA, Salem R, Gaeta AL, Lipson M. Frequency conversion over two-thirds of an octave in silicon nanowaveguides. Opt Express 2010;18:1904–8.

[99] Lau RK, Ménard M, Okawachi Y, et al. Continuous-wave mid-infrared frequency conversion in silicon nanowaveguides. Opt Lett 2011;36:1263–5.

[100] Foster MA, Turner AC, Salem R, Lipson M, Gaeta AL. Broad-band continuous-wave parametric wavelength conversion in silicon nanowaveguides. Opt Express 2007;15:12949–58.

[101] Liu X, Kuyken B, Green WMJ, Osgood RM, Baets R, Roelkens G. Mid-infrared nonlinear silicon photonics. In: Conference on Silicon Photonics IX, vol. 8990. SPIE, 2014.

[102] Kuyken B, Liu X, Roelkens G, Baets R, Osgood Jr RM, Green WM. 50 dB Parametric on-chip gain in silicon photonic wires. Opt Lett 2011;36:4401–3.

[103] Liu X, Osgood RM, Vlasov YA, Green WM. Mid-infrared optical parametric amplifier using silicon nanophotonic waveguides. Nat Photonics 2010;4:557–60.

[104] Kippenberg TJ, Holzwarth R, Diddams S. Microresonator-based optical frequency combs. Science 2011;332:555–9.

[105] Yu M, Okawachi Y, Griffith AG, Lipson M, Gaeta AL. Mode-locked mid-infrared frequency combs in a silicon microresonator. Optica 2016;3:854–60.

[106] Okawachi Y, Saha K, Levy JS, Wen YH, Lipson M, Gaeta AL. Octave-spanning frequency comb generation in a silicon nitride chip. Opt Lett 2011;36:3398–400.

[107] Griffith AG, Yu M, Okawachi Y, et al. Coherent mid-infrared frequency combs in silicon-microresonators in the presence of Raman effects. Opt Express 2016;24:13044–50.

[108] Herr T, Brasch V, Jost JD, et al. Temporal solitons in optical microresonators. Nat Photonics 2014;8:145–52.

[109] Bao C, Zhang L, Matsko A, et al. Nonlinear conversion efficiency in Kerr frequency comb generation. Opt Lett 2014;39:6126–9.

[110] Alfano RR. The supercontinuum laser source: the ultimate white light. Springer, 2016.

[111] Dudley JM, Taylor JR. Supercontinuum generation in optical fibers. Cambridge University Press, 2010.

[112] Kuyken B, Liu X, Osgood RM, Baets R, Roelkens G, Green WM. Mid-infrared to telecom-band supercontinuum generation in highly nonlinear silicon-on-insulator wire waveguides. Opt Express 2011;19:20172–81.

[113] Sun H, Wang K-Y, Salem R, Fendel P, Foster AC. Coherent mid-IR supercontinuum generation in a hydrogenated amorphous silicon waveguide. In: CLEO: Science and Innovations, Optical Society of America, 2015, pp. SM1P.6.

[114] Singh N, Hudson DD, Yu Y, et al. Midinfrared supercontinuum generation from 2 to 6 μm in a silicon nanowire. Optica 2015;2:797–802.

[115] Yu Y, Gai X, Ma P, et al. Experimental demonstration of linearly polarized 2–10 μm supercontinuum generation in a chalcogenide rib waveguide. Opt Lett 2016;41:958–61.

[116] Camacho-Aguilera RE, Cai Y, Patel N, et al. An electrically pumped germanium laser. Opt Express 2012;20:11316–20.

[117] Chen S, Li W, Wu J, et al. Electrically pumped continuous-wave III–V quantum dot lasers on silicon. Nat Photonics 2016;10:307–11.

[118] Rodriguez J, Cerutti L, Grech P, Tournié E. Room-temperature operation of a 2.25 μm electrically pumped laser fabricated on a silicon substrate. Appl Phys Lett 2009;94:061124.

[119] Reboul J-R, Cerutti L, Rodriguez J-B, Grech P, Tournié E. Continuous-wave operation above room temperature of GaSb-based laser diodes grown on Si. Appl Phys Lett 2011;99:121113.

[120] Wirths S, Geiger R, Von Den Driesch N, et al. Lasing in direct-bandgap GeSn alloy grown on Si. Nat Photonics 2015;9:88–92.

[121] Stange D, Wirths S, Geiger R, et al. Optically pumped GeSn microdisk lasers on Si. ACS Photonics 2016;3:1279–85.

[122] Al-Kabi S, Ghetmiri SA, Margetis J, et al. An optically pumped 2.5 μm GeSn laser on Si operating at 110 K. Appl Phys Lett 2016;109:171105.

[123] Reboud V, Gassenq A, Pauc N, et al. Optically pumped GeSn micro-disks with 16% Sn lasing at 3.1 μm up to 180K. arXiv preprint arXiv:1704.06436, 2017.

[124] Weng B, Ma J, Wei L, et al. Room temperature mid-infrared surface-emitting photonic crystal laser on silicon. Appl Phys Lett 2011;99:221110.

[125] Fill M, Khiar A, Rahim M, Felder F, Zogg H. PbSe quantum well mid-infrared vertical external cavity surface emitting laser on Si-substrates. J Appl Phys 2011;109:093101.

[126] Rahim M, Fill M, Felder F, Chappuis D, Corda M, Zogg H. Mid-infrared PbTe vertical external cavity surface emitting laser on Si-substrate with above 1 W output power. Appl Phys Lett 2009;95:241107.

[127] Cornet C, Léger Y, Robert C. Integrated lasers on silicon. Elsevier, 2016.

[128] Paul DJ. The progress towards terahertz quantum cascade lasers on silicon substrates. Laser Photon Rev 2010;4:610–32.

[129] Jeong KS, Guyot-Sionnest P. Mid-infrared photolumines-cence of CdS and CdSe colloidal quantum dots. ACS Nano 2016;10:2225–31.

[130] Fohrmann LS, Petrov AY, Lang S, Jalas D, Krauss TF, Eich M. Single mode thermal emission. Opt Express 2015;23:27672–82.

[131] Kim YD, Kim H, Cho Y, et al. Bright visible light emission from graphene. Nat Nanotechnol 2015;10:676–81.

[132] Lancaster A, Cook G, McDaniel SA, et al. Mid-infrared laser emission from Fe: ZnSe cladding waveguides. Appl Phys Lett 2015;107:031108.

[133] Macdonald J, Beecher S, Berry P, Schepler K, Kar A. Compact mid-infrared Cr: ZnSe channel waveguide laser. Appl Phys Lett 2013;102:161110.

[134] Berry PA, Macdonald JR, Beecher SJ, McDaniel SA, Schepler KL, Kar AK. Fabrication and power scaling of a 1.7 W Cr: ZnSe waveguide laser. Opt Mater Express 2013;3:1250–8.

[135] Wu J, Jiang S, Qua T, Kuwata-Gonokami M, Peyghambarian N. 2 μm Lasing from highly thulium doped tellurite glass microsphere. Appl Phys Lett 2005;87:211118.

[136] Vlasenko NA, Oleksenko PF, Mukhlyo MA, Denisova ZL, Veligura LI. ZnS: Cr and ZnSe: Cr thin-film waveguide structures as electrically pumped laser media with an impact excitation mechanism. Ann Phys 2013;525:889–905.

[137] Madden SJ, Vu KT. High-performance integrated optics with tellurite glasses: status and prospects. Int J Appl Glass Sci 2012;3:289–98.

[138] Vu K, Madden S. Tellurium dioxide Erbium doped planar rib waveguide amplifiers with net gain and 2.8 dB/cm internal gain. Opt Express 2010;18:19192–200.

[139] Lin PT, Vanhoutte M, Patel NS, et al. Engineering broadband and anisotropic photoluminescence emission from rare earth doped tellurite thin film photonic crystals. Opt Express 2012;20:2124–35.

[140] Ogbuu O, Du Q, Lin H, et al. Impact of stoichiometry on structural and optical properties of sputter deposited multicomponent tellurite glass films. J Am Ceram Soc 2015;98: 1731–8.

[141] Jackson SD. Towards high-power mid-infrared emission from a fibre laser. Nat Photonics 2012;6:423–31.

[142] Lin H, Song Y, Huang Y, et al. Chalcogenide glass-on-graphene photonics. Nat Photonics 2017. doi: 10.1038/s41566-017-0033-z.

[143] Vlasov YA, O'boyle M, Hamann HF, McNab SJ. Active control of slow light on a chip with photonic crystal waveguides. Nature 2005;438:65–9.

[144] Nedeljkovic M, Stankovic S, Mitchell CJ, et al. Mid-infrared thermo-optic modulators in SoI. IEEE Photonics Technol Lett 2014;26:1352–5.

[145] Malik A, Dwivedi S, Van Landschoot L, et al. Ge-on-Si and Ge-on-SOI thermo-optic phase shifters for the mid-infrared. Opt Express 2014;22:28479–88.

[146] Zou Y, Chakravarty S, Chung C-J, Chen RT. Miniature mid-infrared thermooptic switch with photonic crystal waveguide based silicon-on-sapphire Mach–Zehnder interferometers. In: Proc. of SPIE Vol, vol. 9753, 2016, pp. 97530Q-1.

[147] Van Campenhout J, Green WM, Assefa S, Vlasov YA. Integrated NiSi waveguide heaters for CMOS-compatible silicon thermo-optic devices. Opt Lett 2010;35:1013–5.

[148] Weigel PO, Savanier M, DeRose CT, et al. Lightwave circuits in lithium niobate through hybrid waveguides with silicon photonics. Sci Rep 2016;6:22301.

[149] Rabiei P, Ma J, Khan S, Chiles J, Fathpour S. Heterogeneous lithium niobate photonics on silicon substrates. Opt Express 2013:21:25573–81.

[150] Chiles J, Fathpour S. Mid-infrared integrated waveguide modulators based on silicon-on-lithium-niobate photonics. Optica 2014;1:350–5.

[151] Jacobsen RS, Andersen KN, Borel PI, et al. Strained silicon as a new electro-optic material. Nature 2006;441:199.

[152] Chmielak B, Waldow M, Matheisen C, et al. Pockels effect based fully integrated, strained silicon electro-optic modulator. Opt Express 2011;19:17212–9.

[153] LiNbO₃ Data Sheet. (Accessed August 14, 2017, at http://www.lambdaphoto.co.uk/pdfs/Inrad_datasheet_LNB.pdf).

[154] Nedeljkovic M, Soref R, Mashanovich GZ. Free-carrier electro-refraction and electro-absorption modulation predictions for silicon over the 1-14μm infrared wavelength range. IEEE Photonics J 2011;3:1171–80.

[155] Nedeljkovic M, Soref R, Mashanovich GZ. Predictions of free-carrier electroabsorption and electrorefraction in germanium. IEEE Photonics J 2015;7:1–14.

[156] Van Camp MA, Assefa S, Gill DM, et al. Demonstration of electrooptic modulation at 2165 nm using a silicon Mach-Zehnder interferometer. Opt Express 2012;20:28009–16.

[157] Thomson D, Shen L, Ackert JJ, et al. Optical detection and modulation at 2 μm-2.5 μm in silicon. Opt Express 2014;22:10825–30.

[158] Shen L, Healy N, Mitchell CJ, et al. Mid-infrared all-optical modulation in low-loss germanium-on-silicon waveguides. Opt Lett 2015;40:268–71.

[159] Li T, Nedeljkovic M, Hattasan N, et al. In: 2017 IEEE 14th International Conference on, IEEE, Mid-Infrared Ge-on-Si electro-absorption modulator, Group IV Photonics (GFP). p WB.3.

[160] Soref R, Sun G, Cheng H. Franz-Keldysh electro-absorption modulation in germanium-tin alloys. J Appl Phys 2012;111:123113.

[161] Zhang Q, Liu Y, Yan J, Zhang C, Hao Y, Han G. Theoretical investigation of tensile strained GeSn waveguide with Si 3 N 4 liner stressor for mid-infrared detector and modulator applications. Opt Express 2015;23:7924–32.

[162] Lin C, Grassi R, Low T, Helmy AS. Multilayer black phosphorus as a versatile mid-infrared electro-optic material. Nano Lett 2016;16:1683–9.

[163] Whitney WS, Sherrott MC, Jariwala D, et al. Field effect opto-electronic modulation of quantum-confined carriers in black phosphorus. Nano Lett 2016;17:78–84.

[164] Peng R, Khaliji K, Youngblood N, Grassi R, Low T, Li M. Mid-infrared electro-optic modulation in few-layer black phosphorus. Nano Lett 2017;17:6315–20.

[165] Dalir H, Xia Y, Wang Y, Zhang X. A thermal broadband graphene optical modulator with 35 GHz speed. ACS Photonics 2016;3:1564–8.

[166] Hanson GW. Dyadic Green's functions and guided surface waves for a surface conductivity model of graphene. J Appl Phys 2008;103:064302.

[167] AMTIR-6 Information. (Accessed August 15, 2017, at http://www.amorphousmaterials.com/app/download/6552919404/AMTIR-6+Information.pdf).

[168] Dereniak EL, Boreman GD. Infrared detectors and systems. Wiley, 1996.

[169] Kinch MA. State-of-the-art infrared detector technology. Bellingham, SPIE Press, 2014.

[170] Rogalski A. Recent progress in infrared detector technologies. Infrared Phys Technol 2011;54:136–54.

[171] Rogalski A. Progress in focal plane array technologies. Prog Quantum Electron 2012;36:342–473.

[172] Ahn D. Intrachip clock signal distribution via si-based optical interconnect. Massachusetts Institute of Technology, 2007.

[173] Hattasan N, Gassenq A, Cerutti L, Rodriguez JB, Tournié E, Roelkens G. Heterogeneous integration of GaInAsSb pin photodiodes on a silicon-on-insulator waveguide circuit. IEEE Photonics Technol Lett 2011;23:1760–2.

[174] Gassenq A, Hattasan N, Cerutti L, Rodriguez JB, Tournié E, Roelkens G. Study of evanescently-coupled and grating-assisted GaInAsSb photodiodes integrated on a silicon photonic chip. Opt Express 2012;20:11665–72.

[175] Ryckeboer E, Gassenq A, Muneeb M, et al. Silicon-on-insulator spectrometers with integrated GaInAsSb photodiodes for wide-band spectroscopy from 1510 to 2300 nm. Opt Express 2013;21:6101–8.

[176] Wang R, Muneeb M, Sprengel S, et al. III-V-on-silicon 2-μm-wavelength-range wavelength demultiplexers with heterogeneously integrated InP-based type-II photodetectors. Opt Express 2016;24:8480–90.

[177] Wang R, Sprengel S, Muneeb M, et al. 2 μm Wavelength range InP-based type-II quantum well photodiodes heterogeneously integrated on silicon photonic integrated circuits. Opt Express 2015;23:26834–41.

[178] Muneeb M, Vasiliev A, Ruocco A, et al. III-V-on-silicon integrated micro-spectrometer for the 3 μm wavelength range. Opt Express 2016;24:9465–72.

[179] Han Z, Singh V, Kita D, et al. On-chip chalcogenide glass waveguide-integrated mid-infrared PbTe detectors. Appl Phys Lett 2016;109:071111.

[180] Wang X, Cheng Z, Xu K, Tsang HK, Xu J-B. High-responsivity graphene/silicon-heterostructure waveguide photodetectors. Nat Photonics 2013;7:888–91.

[181] Souhan B, Grote RR, Chen CP, et al. Si+-implanted Si-wire waveguide photodetectors for the mid-infrared. Opt Express 2014;22:27415–24.

[182] Grote RR, Souhan B, Ophir N, et al. Extrinsic photodiodes for integrated mid-infrared silicon photonics. Optica 2014;1:264–7.

[183] Souhan B, Chen CP, Lu M, et al. Ar+-implanted si-waveguide photodiodes for mid-infrared detection. Photonics 2016;3:46.

[184] Ackert JJ, Thomson DJ, Shen L, et al. High-speed detection at two micrometres with monolithic silicon photodiodes. Nat Photonics 2015;9:393–6.

[185] Fain R, Miller S, Yu M, Griffith AG, Cardenas J, Lipson M. In: CMOS-compatible mid-infrared silicon detector, CLEO: Science and Innovations. Optical Society of America, 2017, p STu1N. 4.

[186] Wang J, Zens T, Hu J, Becla P, Kimerling LC, Agarwal AM. Monolithically integrated, resonant-cavity-enhanced dual-band mid-infrared photodetector on silicon. Appl Phys Lett 2012;100:211106.

[187] Wang J, Hu J, Becla P, Agarwal AM, Kimerling LC. Resonant-cavity-enhanced mid-infrared photodetector on a silicon platform. Opt Express 2010;18:12890–6.

[188] Heves E, Ozturk C, Ozguz V, Gurbuz Y. Solution-based PbS photodiodes, integrable on ROIC, for SWIR detector applications. IEEE Electron Device Lett 2013;34:662–4.

[189] Wang J, Hu J, Sun X, et al. Structural, electrical, and optical properties of thermally evaporated nanocrystalline PbTe films. J Appl Phys 2008;104:053707.

[190] Wang J, Hu J, Becla P, Agarwal AM, Kimerling LC. Room-temperature oxygen sensitization in highly textured, nanocrystalline PbTe films: a mechanistic study. J Appl Phys 2011;110:083719.

[191] Hu JJ, Tarasov V, Carlie N, et al. Si-CMOS-compatible lift-off fabrication of low-loss planar chalcogenide waveguides. Opt Express 2007;15:11798–807.

[192] Wang J. Resonant-cavity-enhanced multispectral infrared photodetectors for monolithic integration on silicon. Massachusetts Institute of Technology, 2010.

[193] Li H, Brouillet J, Salas A, Wang X, Liu J. Low temperature growth of high crystallinity GeSn on amorphous layers for advanced optoelectronics. Opt Mater Express 2013;3:1385–96.

[194] Lhuillier E, Keuleyan S, Zolotavin P, Guyot-Sionnest P. Mid-Infrared HgTe/As2S3 field effect transistors and photodetectors. Adv Mater 2013;25:137–41.

[195] Berencén Y, Prucnal S, Liu F, et al. Room-temperature short-wavelength infrared Si photodetector. Sci Rep 2017;7. Article number 43688.

[196] Simmons CB, Akey AJ, Mailoa JP, Recht D, Aziz MJ, Buonassisi T. Enhancing the infrared photoresponse of silicon by controlling the Fermi level location within an impurity band. Adv Funct Mater 2014;24:2852–8.

[197] Youngblood N, Chen C, Koester SJ, Li M. Waveguide-integrated black phosphorus photodetector with high responsivity and low dark current. Nat Photonics 2015;9:247–52.

[198] Liu B, Köpf M, Abbas AN, et al. Black arsenic–phosphorus: layered anisotropic infrared semiconductors with highly tunable compositions and properties. Adv Mater 2015;27:4423–9.

[199] Long M, Gao A, Wang P, et al. Room temperature high-detectivity mid-infrared photodetectors based on black arsenic phosphorus. Sci Adv 2017;3. Article number e1700589.

[200] Wang Y, Qiu G, Wang Q, et al. Large-area solution-grown 2D tellurene for air-stable, high-performance field-effect transistors. arXiv preprint arXiv:1704.06202, 2017.

[201] Huang Y, Tien EK, Gao S, et al. Electrical signal-to-noise ratio improvement in indirect detection of mid-IR signals by wavelength conversion in silicon-on-sapphire waveguides. Appl Phys Lett 2011;99:181122.

[202] Liu X, Kuyken B, Roelkens G, Baets R, Osgood Jr RM, Green WM. Bridging the mid-infrared-to-telecom gap with silicon nanophotonic spectral translation. Nat Photonics 2012;6:667–71.

[203] Kita D, Lin H, Agarwal A, et al. On-chip infrared spectroscopic sensing: redefining the benefits of scaling. IEEE J Sel Topics Quantum Electron 2017;23:5900110.

[204] Nedeljkovic M, Velasco AV, Khokhar AZ, Delâge A, Cheben P, Mashanovich GZ. Mid-infrared silicon-on-insulator Fourier-transform spectrometer chip. IEEE Photonics Technol Lett 2016;28:528–31.

[205] NIRQuest512-2.5. (Accessed August 20, 2017, at https://oceanoptics.com/product/nirquest512-2-5/).

[206] Muneeb M, Chen X, Verheyen P, et al. Demonstration of Silicon-on-insulator mid-infrared spectrometers operating at 3.8 μm. Opt Express 2013;21:11659–69.

[207] Hu Y, Li T, Thomson DJ, et al. Mid-infrared wavelength division (de) multiplexer using an interleaved angled multimode interferometer on the silicon-on-insulator platform. Opt Lett 2014;39:1406–9.

[208] Barritault P, Brun M, Labeye P, et al. Design, fabrication and characterization of an AWG at 4.5 μm. Opt Express 2015;23:26168–81.

[209] Koshkinbayeva A, Barritault P, Ortiz S, et al. Impact of non-central input in N×M mid-IR arrayed waveguide gratings integrated on Si. IEEE Photonics Technol Lett 2016;28:2191–4.

[210] Chao, T-H, Lu TT, Davis SR, et al. Compact liquid crystal waveguide based Fourier transform spectrometer for in-situ and remote gas and chemical sensing. In: Optical Pattern Recognition XIX, vol. 6977, International Society for Optics and Photonics, 2008, p. 69770P.

[211] Dong B, Cai H, Gu YD, et al. In: 2015 Conference on, 2015, Nano-silicon-photonic fourier transform infrared (FTIR) spectrometer-on-a-chip, Lasers and Electro-Optics (CLEO), IEEE, pp 1-2.

[212] Chen Y, Lin H, Hu J, Li M. Heterogeneously integrated silicon photonics for the mid-infrared and spectroscopic sensing. ACS Nano 2014;8:6955–61.

[213] Harwit M, Sloane NJ. Hadamard transform optics. 1979.

[214] Gutierrez-Arroyo A, Baudet E, Bodiou L, et al. Theoretical study of an evanescent optical integrated sensor for multipurpose detection of gases and liquids in the Mid-Infrared. Sens Actuators B Chem 2017;242:842–8.

[215] Hodgkinson J, Tatam RP. Optical gas sensing: a review. Meas Sci Technol 2012;24:012004.

[216] Zhang EJ, Tombez L, Orcutt JS, Kamlapurkar S, Wysocki G, Green WM. In: Conference on lasers and electro-optics, Silicon photonic on-chip trace-gas spectroscopy of methane, San Jose, California, Optical Society of America, San Jose, California (Accessed June 5, 2016, at p SF2H.1).

[217] VPL Molecular Spectroscopic Database. (Accessed August 25, 2017, at http://vpl.astro.washington.edu/spectra/hydrocarbons.htm).

[218] Hu J. Ultra-sensitive chemical vapor detection using micro-cavity photothermal spectroscopy. Opt Express 2010;18:22174–86.

[219] Lin H, Zou Y, Hu J. Double resonance 1-D photonic crystal cavities for single-molecule mid-infrared photothermal spectroscopy: theory and design. Opt Lett 2012;37:1304–6.

[220] Vasiliev A, Malik A, Muneeb M, Kuyken B, Baets R, Roelkens G. On-chip mid-infrared photothermal spectroscopy using suspended silicon-on-insulator microring resonators. ACS Sens 2016;1:1301–7.